THE CALCULATION OF ROTOR/FUSELAGE INTERACTION FOR TWO-DIMENSIONAL BODIES

Paul M. Stremel
NASA Ames Research Center
Moffett Field, CA 94035-1000

Abstract

Unsteady rotor wake interactions with the empennage, tail boom, and other aerodynamic surfaces have a significant influence on the aerodynamic performance of the helicopter, ride quality, and vibration. A Computational Fluid Dynamic (CFD) method for computing the aerodynamic interaction between an interacting vortex wake and the viscous flow about arbitrary two-dimensional bodies has been developed to address this helicopter problem. The vorticity and flow field velocities are calculated on a body-fitted computational mesh using an uncoupled iterative solution. The interacting vortex wake is represented by an array of discrete vortices which, in turn, are represented by a finite-core model. The evolution of the interacting vortex wake is calculated by Lagrangian techniques. The flow around circular and elliptic cylinders in the absence of an interacting vortex wake has been calculated. These results compare very well with other numerical results and with results obtained from experiment and thereby demonstrate the accuracy of the viscous solution. The interaction of a simulated rotor wake with the flow about two-dimensional bodies, representing cross-sections of fuselage components, has been calculated to address the vortex-interaction problem. The vortex interaction was calculated for the flow about a circular and an elliptic cylinder at 45 and 90 degrees incidence. The results demonstrate the significant variation in lift and drag on the two-dimensional bodies during the vortex interaction.

Symbols

C_d = drag coefficient

C_{fx} = force coefficient in x-direction

C_{fy} = force coefficient in y-direction

C_l = lift coefficient

h_ξ = vector length in transformed space

h_η = vector length in transformed space

J = transformation Jacobian

l = body length

n = time step index, shedding frequency

P = transformation parameter

p = pressure

Q = transformation parameter

r = radial variable

r_c = vortex core radius

r_o = vortex core outer radius

R_e = Reynolds number, U_∞ l/ν

S_t = Strouhal number, nl/U_∞

t = time

U = free stream velocity

u = velocity component in x-direction

v = velocity component in y-direction

x = Cartesian coordinate

y = Cartesian coordinate

α = incidence angle

β = transformation parameter

Δ = incremental value

Γ = circulation

η = coordinate in transformed space

ν = kinematic viscosity

ξ = coordinate in transformed space

ω = vorticity

Subscripts

vw = interacting vortex wake quantity

o = reference value

1 = value at body surface

∞ = value at far field

Introduction

The numerical prediction for the strong interaction between vortical wakes and the viscous flow field about bodies is of considerable importance in the design analysis of rotorcraft. The flow field surrounding a helicopter configuration is highly complex due to the lack of symmetry and the unsteady aspects of the flow. This unsteady, asymmetric flow field is complicated further in that the shed wake from the rotor blades interacts with other components of the aircraft (e.g., rotor blades, fuselage, tail boom, and tail rotor). In general, these are strong interactions in which the rotor wake flows onto or passes very close to the other components of the aircraft. Vortex interactions occur at many flight attitudes (e.g., hover, descent, and low speed flight) and therefore have profound effects on the overall aerodynamic efficiency of the rotorcraft. The effects of the vortex interactions are realized as increased vibratory loading on the fuselage, decreased payload capabilities, and increased noise.

Because of the complexity of the problem and the limitations of the computer in modeling the entire flow field, the research effort addressing vortex interaction for rotorcraft has developed in two directions: blade-vortex interaction and rotor-fuselage interaction. Most of the vortex-interaction research for rotorcraft has been directed toward blade-vortex interaction in forward flight and, therefore, concentrated on the flow field near the rotor tip on the advancing side of the rotor. The flow field in this region is transonic and the rotor blade is at near zero incidence. Navier-Stokes calculations of blade-vortex interaction are being conducted with increasing efficiency (Refs 1, 2). These calculations model limited separation, due to the incidence of the blade and flow velocity. In addition, the blade-vortex interaction is generally not a direct interaction between the rotor blade and the rotor wake, but a very close passage. Aircraft descent is the exception when the rotor wake is convected through the rotor and directly interacts with the rotor blades. The flow beneath the rotor is quite different, with rotor-fuselage interactions present over a large portion of the fuselage length.

The rotor-fuselage interaction has received far less attention than that for the blade-vortex interaction. These interactions, which exist for most flight configurations, are caused by the impingement of the convected rotor wake onto the fuselage components. An overview of the rotor-fuselage interactional aerodynamics can be found in Ref. 3. In contrast to the blade-vortex interaction, the flow field of the rotor-fuselage interaction is subsonic, highly separated, and vortex dominated. Portions of the fuselage are immersed in the rotor downwash, which is an unsteady flow with very large velocity gradients just inboard of the rotor tip. The fuselage is not streamlined in the direction of the downwash; as a consequence, separated wakes form at the surface owing to viscosity. These separated wakes are very unsteady due to the interaction of the impinging rotor wake. The result of the vortex interaction is the coupling of the vorticity produced at the surface of the fuselage with the interacting vortex wake. The flow becomes increasingly unsteady due to the mutual convection between the interacting vortex wake and the surface vorticity. The resulting flow field is very complex, and therefore difficult to model and predict.

The analysis of rotor-fuselage interactions, as well as blade-vortex interactions, is complicated further by computer memory limitations. Currently available computer memory is inadequate for the three-dimensional meshes necessary to model the flow field surrounding a representative rotorcraft. Therefore, the computational mesh enclosing a body is generally concentrated near the body to resolve the flow at that location and considerably less dense away from the body. Owing to numerical diffusion, the coarse mesh away from the body is inadequate for accurate predictions for the evolution of the rotor wake surrounding a rotorcraft. In order to calculate the rotor-fuselage interaction, a method is needed to accurately predict both the rotor wake evolution away from the body on a coarse mesh and the separated viscous flow near the body surface.

As a first step toward analyzing the full three-dimensional rotor-fuselage interaction, this paper presents a method to calculate the unsteady, two-dimensional, incompressible interaction of an interacting vortex wake with the separated flow about bodies. The method solves the velocity/vorticity formulation of the Navier-Stokes equations. The computational mesh is concentrated near the body surface to resolve the boundary layer and is increasingly coarse further from the body. The interacting vortex wake is modeled as an array of finite-core vortices (Refs 4, 5). The core radius is variable and is independent of the mesh spacing. The finite-core model eliminates the numerical diffusion associated with the coarse mesh spacing away from the body and provides for the accurate prediction of the rotor wake evolution. The finite-core vortex model is accurate away from the body where the flow field is inviscid and dominated by the rotor wake. However, closer to the body, the flow is viscous and the convection of the rotor wake can no longer be considered inviscid. In this region, the interacting vortex wake interacts with the viscous separated wake and can no longer be modeled by the finite-core vortex model. The vortex core is acted upon by shearing forces which will

contort and possibly separate the vortex core into several separate vortices. As the vortex approaches the body, the finite-core vortex is distributed to the computational mesh and allowed to convect as part of the viscous solution. In this way the evolution of the rotor wake away from the body and the vortex interaction at the body are accurately simulated. In addition the present method for two-dimensional calculations is directly extendable to three-dimensional analysis.

Results for the viscous flow about two-dimensional bodies have been calculated with and without an interacting vortex wake. The flow around circular and elliptic cylinders in the absence of an interacting vortex wake has been calculated in order to compare results of the current method with those of other numerical studies and experimental investigations. The intent of this paper is to provide comparisons between the flow about bodies with and without the presence of an interacting vortex wake. The simulated flow represents the downwash beneath a rotor. In this two-dimensional analysis, the body represents a cross-section of the tail boom or fuselage component, which may be circular or elliptical in geometry.

Problem Formulation

The vortex interaction problem is modeled by the velocity/vorticity form of the unsteady incompressible Navier-Stokes equations. The nondimensional governing equations in Cartesian coordinates are written: for the velocity,

$$\nabla^2 u = -\partial\omega/\partial y \,,\ \nabla^2 v = \partial\omega/\partial x \qquad (1a,b)$$

and for the vorticity,

$$\omega_t + \partial(u\omega)/\partial x + \partial(v\omega)/\partial y = \nabla^2\omega/R_e \qquad (2)$$

where $\nabla^2 = \partial^2(\,)/\partial x^2 + \partial^2(\,)/\partial y^2$

where (x,y) are the Cartesian coordinates, R_e is the Reynolds number, and t is the time. The variables (u,v) are the Cartesian components of the velocity and ω, the vorticity, is defined by

$$\omega = \partial v/\partial x - \partial u/\partial y \qquad (3)$$

The nondimensional variables are written

$$x = x'/l,\ y = y'/l,\ u = u'/U_\infty,\ v = v'/U_\infty$$

$$\omega = \omega'/(U_\infty/l),\ t = t'/(l/U_\infty),\ R_e = U_\infty l/\nu$$

where

l = the body length

R_e = Reynolds number based on body length

U_∞ = free stream velocity

ν = kinematic viscosity

A body fitted computational mesh is used in the finite-difference solution to the governing equations. A hyperbolic mesh generator was used to generate the computational mesh, Ref 6. A portion of the computational mesh is shown in Fig 1. The solution to the flow is obtained by solving the transformed Cartesian equations in the computational domain (ξ,η).

The general transformation expression can be written, via the chain rule, as

$$\partial(\,)/\partial\xi = \partial x/\partial\xi(\partial(\,)/\partial x) + \partial y/\partial\xi(\partial(\,)/\partial y), \text{ and}$$

$$\partial(\,)/\partial\eta = \partial x/\partial\eta(\partial(\,)/\partial x) + \partial y/\partial\eta(\partial(\,)/\partial y), \text{ or}$$

$$\begin{bmatrix}\partial()/\partial\xi \\ \partial()/\partial\eta\end{bmatrix} = \begin{bmatrix}\partial x/\partial\xi & \partial y/\partial\xi \\ \partial x/\partial\eta & \partial y/\partial\eta\end{bmatrix}\begin{bmatrix}\partial()/\partial x \\ \partial()/\partial y\end{bmatrix}.$$

The derivatives $\partial(\,)/\partial x$, and $\partial(\,)/\partial y$ are solved for by inverting the coefficient matrix in the above equation. The Cartesian derivatives become

$$\begin{bmatrix}\partial()/\partial x \\ \partial()/\partial y\end{bmatrix} = 1/J\begin{bmatrix}\partial y/\partial\eta & -\partial y/\partial\xi \\ -\partial x/\partial\eta & \partial x/\partial\xi\end{bmatrix}\begin{bmatrix}\partial()/\partial\xi \\ \partial()/\partial\eta\end{bmatrix},$$

where J is the Jacobian of the transformation. This relation is used to transform the derivatives of the governing equations to the generalized curvilinear coordinates. In the computational domain, the governing equations become

for the u-velocity component,

$$h_\eta^2(\partial^2 u/\partial\xi^2) - 2\beta(\partial^2 u/\partial\xi\partial\eta) + h_\xi^2(\partial^2 u/\partial\eta^2) + P\partial u/\partial\xi + Q\partial u/\partial\eta = -J[x_\xi(\partial\omega/\partial\eta) - x_\eta(\partial\omega/\partial\xi)], \qquad (4a)$$

for the v-velocity component,

$$h_\eta^2(\partial^2 v/\partial\xi^2) - 2\beta(\partial^2 v/\partial\xi\partial\eta) + h_\xi^2(\partial^2 v/\partial\eta^2) + P\partial v/\partial\xi + Q\partial v/\partial\eta = -J[y_\eta(\partial\omega/\partial\xi) - y_\xi(\partial\omega/\partial\eta)], \qquad (4b)$$

and for the vorticity,

$$\omega_t + [y_\eta(\partial u\omega/\partial\xi) - y_\xi(\partial u\omega/\partial\eta)]/J$$

$$+ [x_\xi(\partial v\omega/\partial\eta) - x_\eta(\partial v\omega/\partial\xi)]/J$$

$$= [h_\eta^2(\partial^2\omega/\partial\xi^2) - 2\beta(\partial^2\omega/\partial\xi\partial\eta) + h_\xi^2(\partial^2\omega/\partial\eta^2)$$

$$+ P\partial\omega/\partial\xi + Q\partial\omega/\partial\eta]/(R_eJ^2) \qquad (5)$$

where (ξ,η) are the transformed coordinates, h_ξ and h_η are the vector lengths,

$$h_\xi = (x_\xi^2 + y_\xi^2)^{1/2} \text{ and}$$

$$h_\eta = (x_\eta^2 + y_\eta^2)^{1/2}$$

with

$$\beta = x_\xi x_\eta + y_\xi y_\eta,$$

$$J = x_\xi y_\eta - x_\eta y_\xi,$$

$$P = [y_\xi(h_\eta^2 x_{\xi\xi} - 2\beta x_{\xi\eta} + h_\eta^2 x_{\eta\eta})$$

$$- x_\xi(h_\eta^2 y_{\xi\xi} - 2\beta y_{\xi\eta} + h_\eta^2 y_{\eta\eta})]/J,$$

$$Q = [-y_\eta(h_\eta^2 x_{\xi\xi} - 2\beta x_{\xi\eta} + h_\eta^2 x_{\eta\eta})$$

$$+ x_\eta(h_\eta^2 y_{\xi\xi} - 2\beta y_{\xi\eta} + h_\eta^2 y_{\eta\eta})]/J,$$

and

$$x_\xi = \partial x/\partial\xi,\ x_\eta = \partial x/\partial\eta,\ y_\xi = \partial y/\partial\xi,\ y_\eta = \partial y/\partial\eta,$$

$$x_{\xi\xi} = \partial^2 x/\partial\xi^2,\ x_{\eta\eta} = \partial^2 x/\partial\eta^2,\ y_{\xi\xi} = \partial^2 y/\partial\xi^2,$$

$$y_{\eta\eta} = \partial^2 y/\partial\eta^2$$

The boundary conditions for Eqs 4a, 4b, and 5 at the body surface are calculated from the no-slip condition as

$$u = 0,\ v = 0 \qquad (6)$$

and the definition of vorticity for ω,

$$\omega = [y_\eta\partial v/\partial\xi + x_\eta\partial u/\partial\xi]/J \qquad (7)$$

The boundary conditions at the far field boundary are

$$u = U_\infty\cos(\alpha) \qquad (8a)$$

$$v = U_\infty\sin(\alpha) \qquad (8b)$$

and

$$\omega = 0 \qquad (9)$$

in the potential flow region upstream of the body, i.e., for $\eta_1 < \eta < \eta_2$ of Fig 1, with η increasing in the counter-clockwise direction.

In the region downstream of the body, the velocity at the far field boundary is calculated from Eqs 4a and 4b and the vorticity is calculated from Eq 5 by considering the inertia terms only and neglecting the viscous terms. Therefore, the vorticity at the far field boundary, for $\eta_2 < \eta < \eta_{max}$ and $\eta_{min} < \eta < \eta_1$ is calculated from

$$\omega_t + [y_\eta(\partial u\omega/\partial\xi) - y_\xi(\partial u\omega/\partial\eta)]/J$$

$$+ [x_\xi(\partial v\omega/\partial\eta) - x_\eta(\partial v\omega/\partial\xi)]/J = 0. \qquad (10)$$

The surface pressure is obtained by integrating the tangential component of the Navier-Stokes equation along the surface of the body. At the surface

$$p_\eta = -[(\beta\omega_\eta - h_\eta^2(\partial\omega/\partial\xi)]/(ReJ) \qquad (11)$$

or

$$p_1 = p_o - 1/R_e\int_{\eta_o}^{\eta_1}[\beta\omega_\eta - h_\eta^2(\partial\omega/\partial\xi)/J]d\eta \qquad (12)$$

where p_1 is the pressure on the surface and p_o is the reference pressure on the surface.

The reference pressure is obtained by the line integral of the momentum equation from the far field boundary to the body surface along a constant η line. The reference pressure is calculated from

$$p_o = \int_{\xi_1}^{\xi_\infty}[\partial(x_\xi u + y_\xi v)/\partial t - (x_\xi v\omega - y_\xi u\omega)$$

$$+ h_\xi^2(\partial\omega/\partial\eta) - \beta(\partial\omega/\partial\xi)/(R_eJ)]d\xi + 1/2 \qquad (13)$$

The force components acting on the body are calculated from the integration of the pressure and shearing forces at the body surface. The force coefficients are

$$C_{fx} = -\int_{\eta_{min}}^{\eta_{max}}(p_1y_\eta)\,d\eta$$

$$-(1/Re)\int_{\eta_{min}}^{\eta_{max}}(\omega_1x_\eta)d\eta \qquad (14)$$

$$C_{fy} = -\int_{\eta_{min}}^{\eta_{max}} (p_1 x_\eta)\, d\eta$$

$$-(1/Re)\int_{\eta_{min}}^{\eta_{max}} (\omega_1 y_\eta) d\eta \qquad (15)$$

where ω_1 is the vorticity at the body.

The lift and drag coefficients are

$$C_l = -C_{fx}[\sin(\alpha)) + C_{fy}(\cos(\alpha)] \qquad (16)$$

$$C_d = C_{fx}[\cos(\alpha)) + C_{fy}(\sin(\alpha)] \qquad (17)$$

where α is the incidence of the body.

The interacting vortex wake is modeled as an array of finite-core vortices. A third-order-polynomial distribution of vorticity about each vortex position is used to represent the vortex core, Ref 4. This distribution of vorticity is

$$\omega_{VW}(r) = \Gamma/(2\pi r_o^2)[\,20/3(r^3/r_o^3) - 10(r^2/r_o^2) + 10/3] \qquad (18)$$

where ω_{VW} represents the vorticity of the interacting vortex wake and r_o is the outer radius of the vortex distribution. The core radius, r_c, the radial position of maximum tangential velocity, is equal to 0.6376 r_o for this finite-core vortex model. The influence of the interacting vortical wake is included in Eqs (4a) and (4b) through the ξ and η components of $-(\bar{\nabla} \times \bar{\omega}_{VW})$. The interacting vortex wake is modeled as an array of finite-core vortices prior to the interaction. However, when the interacting vortex wake is less than a prescribed distance from the body surface, the finite-core model is no longer adequate to model the wake. At this point, the interacting vortex wake is distributed to the computational mesh and included as part of the viscous solution. In this way the vortex interaction is modeled by the governing equations.

Numerical Method

The governing equations are solved by standard finite difference methods on the body-fitted computational mesh. The mesh is concentrated near the body to resolve the flow at that location. The solution is started impulsively from rest. The impulsive start is represented by a potential velocity distribution in the flow field with zero velocity and a sheet of vorticity at the body surface.

The vorticity transport equation, Eq (5), is solved using an alternating direction implicit method (ADI) (Ref 7). The ADI method solves the time-dependent vorticity transport equation by separating the equation into two implicit equations representing two fractional steps for a single time step. This method results in the solution of scalar tridiagonal matrices for each fractional step.

The vorticity at the body surface in Eq (5) is calculated from Eq (7), The velocity, Eqs (4a) and (4b), are cast in a time-dependent form and solved by the ADI method. The influence of the interacting vortex wake is included in the velocity equations through the negative curl of the vorticity distribution in the vortex core, $-(\bar{\nabla} \times \bar{\omega}_{VW})$. The vorticity distribution in the vortex core is defined in Eq (18). Outside the outer radius the vorticity is zero.

The solution to the time-dependent problem is calculated by solving the vorticity transport equation and the velocity equations in an uncoupled manner. In this way, the vorticity transport equation is solved first, after which each velocity equation is solved in turn. This solution procedure continues until a converged solution is obtained for the current time step. The influence of the interacting vortex wake is considered constant at each time step during this iteration process. At convergence, the vorticity, flow field velocity, and interacting vortex wake position are updated and the solution advances in time.

Computed Results

The method described above has been applied to the flow about a circular cylinder and a 25% elliptic cylinder for a Reynolds number of 3000. The computational grid is dimensioned 81 × 241 with the far field radius $r_\infty = 20$ for all calculations. The time is nondimensionalized with respect to the length of the body, in this case the diameter of the cylinder. Therefore, a time interval of $\Delta t = 1.0$, corresponds to the time required to travel a distance equal to the cylinder diameter at a velocity equal to that of the free stream velocity. The flow is calculated with and without the presence of the interacting vortex wake.

The flows about a circular cylinder and an elliptic cylinder at 45 and 90 degrees incidence are calculated without the interacting vortex wake and are included for comparison with the results of the vortex interaction. The incidence angle is measured with respect to the vertical axis as shown in Fig 1. Comparisons of the results for the circular cylinder without the interacting vortex wake can be found in Ref 8. In this reference comparisons are made between the results of the present method, the experimental results of Ref 9 and the numerical results of Ref 10. In Ref 8, comparisons are made between the current method and the results of

Ref 9 for the surface vorticity and were shown to be excellent. In addition, the velocity profile in the wake of the circular cylinder for the current method was compared with the results of Refs 8 and 9. The comparisons were shown to be excellent.

The flow around a circular cylinder and a 25% elliptic cylinder is calculated during the vortex interaction. The flow about the elliptic cylinder during the vortex interaction was calculated for 45 and 90 degrees incidence with respect to the vertical axis. The flow about the elliptical cylinder at 45 degrees incidence was calculated for a vortex strength of each vortex in the interacting vortex wake of $\Gamma = -1.0$ and $\Gamma = 1.0$. The flow about the circular cylinder and the elliptic cylinder at 90 degrees incidence is only calculated for a vortex strength of each vortex in the interacting vortex wake of $\Gamma = 1.0$ due to symmetry. A vortex of strength $\Gamma = -1$ represents a clockwise rotation, while a vortex of strength $\Gamma = 1$ represents a counterclockwise rotation. These vortex interactions were considered to evaluate general vortex interactions and because no specific experimental data representative of this flow exists.

No Vortex Interaction Case

Circular Cylinder. The variation of the lift and drag coefficients with time for the flow about the circular cylinder are shown in Fig 2. The effect of the secondary vortices on the drag coefficient can be seen as the small variations in the curve. The development of the separated vortices remain symmetric up to $t = 40.0$ and, therefore, the lift coefficient is zero. Comparisons between these results and the results of other investigations can be found in Ref 8. The development of the streamlines of this flow are shown in Fig 3. The figure demonstrates the emergence of secondary vortices downstream of the cylinder. These results will be compared with the results during a vortex interaction presented later in this paper.

Elliptic Cylinder. The time evolution of the lift and drag coefficients for the flow about a 25% elliptic cylinder are shown in Fig 4 for 45 degrees incidence. For t greater than $t = 20.0$, the Strouhal number ($S_t = nl/U_\infty$) for this flow is equal to 0.174 based on the projected body length. The development in time of the streamlines around the elliptic cylinder are shown in Fig 5 for 45 degrees incidence.

Variations in the lift and drag coefficients with time for the flow around an elliptic cylinder at 90 degrees incidence are shown in Fig 6. For this flow the separated vortices do not remain symmetric and begin to oscillate at $t = 5.0$. This is indicated in the nonzero lift coefficient and is shown in the development of the streamlines in Fig 7. The Strouhal number of this flow is equal to 0.214.

Vortex Interaction Case

The interaction of a vortex wake with the flow about a circular cylinder and the flow about a 25% elliptic cylinder are calculated. The interaction of the vortex wake with the flow about the elliptic cylinder was calculated for 45 and 90 degrees incidence with respect to the free stream.

Each interaction modeled the interacting vortex wake as an array of vortices inserted into the flow field at constant time intervals. This represents the periodic passage of a rotor blade and the associated tip vortex, thus generating the rotor's vortical wake structure. The orientation of the interacting vortex wake with respect to the elliptic cylinder is depicted in Fig 8. The free stream velocity is directed along the negative y-axis and represents the downwash due to a rotor. The vortex interaction was started at $t = 0.25$, which was long enough after the impulsive start as not to adversely affect the initial development of the flow. At the start of the interaction, five vortices are inserted in the flow field, as shown in Fig 8. Then, as the interaction proceeds, an additional vortex is repeatedly inserted in the flow field at the uppermost position, $y = 6.5$, at a constant time interval, $\Delta t = 1.0$. Therefore, the interacting vortex wake will represent the periodic rotor wake during the entire vortex interaction.

Circular Cylinder , $\Gamma = 1.0$. The variation in the lift coefficient and drag coefficient during the vortex interaction are shown in Figs 9 and 10, respectively. The immediate effect of the interaction is to rapidly increase the lift on the cylinder, Fig 9a, and slightly reduce the drag, Fig 10a. This increased lift is the result of the induced angle of attack of the cylinder due to the presence of the interacting vortex wake. The lift on the cylinder in the absence of the interacting vortex wake was zero. As the interaction progresses, the effect of the periodic passage of the interacting vortex wake can be seen in the variation in the lift on the cylinder. The lift coefficient rises rapidly and then is reduced quickly in a sawtooth pattern representative of a vortex interaction. The separation in these lift peaks is approximately $t = 1.0$. This corresponds to the natural convection of the vortices at the free stream velocity, $U_\infty = 1.0$. The effect of the vortex interaction on the drag, Fig 10, is less pronounced than that for the lift, Fig 9. At $t = 5.0$ a strong vortex interaction begins to occur. This strong vortex interaction is the result of the initial vortex trajectory taken by the uppermost vortex at the start of the interaction. As the interaction starts, the uppermost vortex trajectory is acted upon by the free stream velocity and the influence of the vortices beneath this position. Because there are no vortices above this position, the vortex is convected in a direction down and to the left. This is indicated in the vortex trajectories of Fig 11 and the development of the streamlines during the

interaction, as shown in Fig 12. In Fig 12e at t = 5.0, a pair of vortices can be seen just above the cylinder surface. The vortex to the left is the vortex that started at the uppermost position and is being convected into the cylinder due to the effect of the vortex to the right. After the strong interaction, the interacting vortex wake has regained the the constant vortex separation similar to the initial distribution of the interacting vortices. However, the vortices of the interacting vortex wake are now convected along a curved trajectory to the left of the initial distribution, as shown in Fig 11b. The lift returns to the sawtooth distribution prior to the strong interaction, Fig 9, t = 6.0. For time t > 20.0, a pattern of periodic vortex shedding from the cylinder is shown in the lift, Fig 9b, and the drag, Fig 10b.

The vortex trajectories during the interaction are shown in Fig 11. The trajectories of the five vortices initially inserted into the flow at t = 0.25 are shown in Fig 11a and the trajectories of the vortices inserted in the flow at y = 6.5 for the duration of the interaction are shown in Fig 11b. The figure indicates that the initial vortex that starts at the uppermost position, y = 6.5, is convected in a direction down and to the left. It is this vortex that generates the strong vortex interaction because it is convected nearest to the cylinder surface owing to the effects of the other vortices. Once the initial vortex at the uppermost position has passed the cylinder, the interacting vortices of the vortex wake convect in a regular pattern along the curved trajectory of Fig 11b.

Development of the streamlines for the vortex interaction are shown in Fig 12. Initially, Fig 12a, t = 1.0, the vortices are aligned in a pattern similar to that of the initial vortex distribution. Later, at t = 2.0, Fig 12b, a vortex has been distributed to the mesh and is shown as the local curvature in the streamlines just above the cylinder surface. At t = 4.0, the vortex that started at the uppermost position, y = 6.5, can be seen near the stagnation streamline and is being convected at an increased rate as to overtake the adjacent vortex. This increased descent is due to the influence of the adjacent vortex. The vortex which started at the uppermost position passes closest to the cylinder surface at t = 6.0 and is the closest approach of any vortex during the vortex interaction. Later on, the vortices of the interacting vortex wake are very regularly spaced and are being convected along the curved trajectory toward the cylinder surface.

Elliptic Cylinder. Several vortex interactions are considered for flow about a 25% elliptic cylinder The differences in the vortex interactions are the result of varying the incidence angle and the rotation sense of the vortices that comprise the interacting vortex wake. The vortex interaction is considered for 45 and 90 degrees incidence. Due to symmetry, a single interaction is considered for the flow at 90 degrees incidence. At 45 degrees incidence, two interactions are considered, the difference being the rotation sense of the vortices in the interacting vortex wake. The three interactions are described below.

First Interaction, $\Gamma = -1.0$, $\alpha = 45°$: The vortex interaction is started at t = 0.25, as before. The variation in the lift and drag coefficients during the vortex interaction are shown in Figs 13 and 14, respectively. The initial effect of the vortex interaction is to rapidly reduce the lift on the elliptic cylinder. The is due to the movement of the stagnation streamline and therefore, a reduction in the induced incidence of the elliptic cylinder. A corresponding reduction in the drag is seen in Fig 14. The reductions in the lift and drag are quickly reversed as the vortex interaction progresses, t = 2.0, and the sawtooth signature in the lift and drag develop. The sawtooth pattern is representative of the passage of the periodic interacting vortex wake over the elliptic cylinder. As in the previous vortex interaction for the circular cylinder, the vortex that starts at the uppermost position, y = 6.5, convects in a direction so as to pass closest to the surface of the elliptic cylinder. During this interaction, the uppermost vortex is convected in a direction down and to the right, which is again toward the stagnation streamline and is caused by the effects of the interacting vortices below the initial vortex position. This is clearly seen in the development of the vortex trajectories of Fig 15 and the development of the streamlines shown in Fig 16. The strong vortex interaction seems to occur at t = 6. At this time a change in the lift, Fig 13, and the drag, Fig 14, is observed. A spike in the loading before t = 4.5 and after t = 8.5 is not present in the lift and drag distribution at t = 6.0 due to the strong vortex interaction. At t = 8.0, the lift, Fig 13, and the drag, Fig 14, return to the sawtooth distribution prior to the strong interaction. As in the previous interaction, the interacting vortex wake has regained the constant vortex separation, as shown in Fig 16, similar to the initial distribution of the interacting vortices, and the vortices are being convected along a curved trajectory. The curved trajectory is now to the right of the initial distribution, as shown in Fig 15b. For t > 20.0 the loading on the elliptic cylinder is periodic. The effect of the vortex interaction can be seen as the "spikes" in the loading.

The vortex trajectories during the interaction are shown in Fig 15, and indicate that the initial vortex which starts at the uppermost position, y = 6.5 is convected in a direction down and to the right, as shown in Fig 15a. It is this vortex that generates the strong vortex interaction because it is convected along trajectories close to the stagnation streamline of the cylinder. This trajectory provides the closest approach to the surface of the elliptic cylinder as shown in the figure. After this interaction, the vortices are convected along the curved trajectory shown in Fig 15b.

Development of the streamlines for the vortex interaction are shown in Fig 16. At the early developments of the interaction, Figs 16a,16b, and 16c (t = 1.0, t = 2.0, and t = 3.0), the vortices are aligned in a pattern similar to that of the initial vortex distribution. When t = 4.0 (Fig 16d) the vortex started at the uppermost position can be seen closest to the stagnation streamline. It is this vortex that will make the closest approach to the cylinder and generate the strong vortex interaction. At t = 5.0, the effect of the adjacent vortex to the left of the vortex started at the uppermost position is shown to convect this vortex toward the cylinder. The interacting vortex wake has a profound effect on the development of the separated wake below the elliptic cylinder. This is most significant at t = 7.0, 8.0, and 9.0, where three separated vortices are in close proximity to the lower surface of the elliptic cylinder. During the developing flow in the absence of the interacting vortex wake (Fig 5), the shed vortices oscillate from leading to trailing edge, thereby generating a vortex street in the wake of the cylinder. This vortex street is altered significantly during the vortex interaction.

Second Interaction, $\Gamma = 1.0$, $\alpha = 45°$: This vortex interaction is calculated because the flow about the elliptic cylinder at 45 degrees incidence is not symmetric with respect to the rotation direction of the vortices in the interacting vortex wake. The vortex interaction is again started at t = 0.25. The vortex strength is now equal to $\Gamma = 1.0$, for each vortex in the interacting vortex wake. This corresponds to a counter-clockwise rotating vortex of magnitude $\Gamma = 1.0$. The variation in the lift and drag coefficients during the vortex interaction are shown in Figs 17 and 18, respectively. During this vortex interaction, the effect of the interacting vortex wake is to significantly increase the lift and drag on the cylinder. This is due to the rotation of the stagnation streamline which increases the induced incidence of the cylinder. At approximately t = 1.5, the sawtooth pattern in the lift and drag can be seen. The pattern is less pronounced during this interaction than the previous interaction because the effect of the interacting vortex wake is less significant in comparison with the vorticity generated at the surface of the elliptic cylinder. The strength of the shed vorticity at the leading edge of the cylinder increases with incidence and will dominate the flow near this location. The sawtooth pattern is fairly consistent for the lift, Fig 17, and for the drag, Fig 18, up to a time of t = 5.5. At this time t = 5.5, the strong vortex interaction is occurring, although not clear from the lift and drag. This strong interaction is again the result of the convection of the uppermost vortex due to the influence of the other interacting vortices and the closest approach of this vortex to the surface of the cylinder. This can be seen in the vortex trajectories of Fig 19 and the streamline contours of Fig 20. The effect of the interacting vortices during the interaction is to first accelerate the flow around the leading edge of the elliptic cylinder and to then retard this flow, Figs 20e and 20f. This has a significant effect on the separated vortex wake generated at that location and, therefore, the vortex wake below the cylinder.

The variation in the drag coefficient on the cylinder during the interaction is shown in Fig 18. As in the previous interaction, Figs 13 and 14, and unlike the interaction of the vortex wake with the circular cylinder, Figs 9 and 10, the lift, Fig 17, and the drag, Fig 18, show similar trends during this interaction. At the early stages of the interaction, t = 1.0, the drag is sharply increased due to the interaction, after which the sawtooth pattern is present, t = 1.5 to t = 5.0. At t = 5.0, the drag is significantly increased due to the strong vortex interaction as was seen in the lift, Fig 17. Later, the sawtooth pattern in the drag reemerges, t > 8.0, Fig 18. Later, Fig 18b, the loading on the cylinder becomes periodic with a Strouhal number similar to that for the flow with no vortex interaction.

The vortex trajectories during the interaction are shown in Fig 19 and indicate that the vortex which starts at the uppermost position, y = 6.5, is convected in a direction down and to the left due to the influence of the other interacting vortices. It is this initial vortex that generates the strong vortex interaction because it is convected along trajectories close to the stagnation streamline of the cylinder and passes closest to the cylinder surface. After this vortex passes the cylinder, the interacting vortices are convected along a curved trajectory, Fig 19b, to the left of the initial distribution.

Development of the streamlines for the vortex interaction are shown in Fig 20. At the early developments of the interaction, Figs 20a, 20b, and 20c (t = 1.0, t = 2.0, and t = 3.0), the vortices are aligned in a pattern similar to that of the initial vortex distribution and have significantly increased the induced incidence of the elliptic cylinder. When t = 4.0 (Fig 20d) the vortex that started at the uppermost position can be seen as the vortex to the left in the figure. At t = 5.0 and t = 6.0, this vortex is close to the surface of the elliptic cylinder and will pass closest to the cylinder. It is this vortex that contributes to the strong vortex interaction.

Third Interaction, $\Gamma = 1.0$, $\alpha = 90°$: The variation in the lift and drag coefficients during the vortex interaction are shown in Figs 21 and 22, respectively. The effect of the interaction is to first increase the lift on the elliptic cylinder, up to t = 6.0, at which time a strong vortex interaction occurs. The sawtooth pattern in the lift, indicative of vortex passage, is again present. In comparing the lift during this interaction, Fig 21, with the lift during the vortex interaction with the circular cylinder, Fig 9, the current interaction generates a less pronounced effect on the lift. This is due to the curvature of the respective cylinders and the effect of the interacting

vortex wake on these surfaces. The variation in the drag during this interaction is shown in Fig 22. The drag is initially increased, but only slightly when compared with the drag for no interaction as shown on the figure. Later, large spikes in the drag distribution are present at t = 2.5, 3.5, 4.5, and 5.5, representing the passage of the interacting vortices. These spikes in the drag distribution are due to the influence of each vortex in the interacting vortex wake. As each vortex approaches the elliptic cylinder, the flow at the upper surface is accelerated resulting in a corresponding reduction in drag. The drag during the interaction nearly returns to the value for no interaction. The strong vortex interaction at t = 6.5 disrupts this effect and suppresses the spike in the drag. At t = 8.0, the strong vortex interaction is over and the drag, Fig 22, begins to return to the distribution shown prior to the interaction. For t > 20.0, the flow becomes periodic with a Strouhal number similar to that for the no-interaction flow.

The vortex trajectories during the interaction are shown in Fig 23 and indicates that the initial vortex which starts at the uppermost position, y = 6.5, is convected in a direction down and to the left due to the influence of the other interacting vortices. This vortex passes close to the upper surface of the cylinder, disrupting the flow at that location, Fig 23a. The interacting vortices are eventually convected along a curved trajectory, Fig 23b, to the left of the initial vortex distribution. Closer to the cylinder, the vortices do not follow a single trajectory, similar to that for the interaction with the flow about a circular cylinder, Fig 11. Instead, the vortex trajectories are fanned out near the surface.

Development of the streamlines for the vortex interaction are shown in Fig 24. At the early developments of the interaction, Figs 24a, 24b, and 24c (t = 1.0, t = 2.0, and t = 3.0), the vortices are again aligned in a pattern similar to that of the initial vortex distribution. The effect of the interacting vortices is to increase the upper surface circulation around the right side of the cylinder. This produces the increase in lift, Fig 21, and the corresponding spikes in the drag, Fig 22 for the passage of each interacting vortex. The strong vortex interaction is shown for times t = 6.0, Fig 24f when the initial vortex at the uppermost position passes closest to the cylinder. Figure 24f clearly shows the effect of the interacting vortex wake on the shed wake below the cylinder when these results are compared with the flow for no interaction, Fig 7.

Conclusions

A method has been developed to model the two-dimensional interaction between an interacting vortex wake represented by a finite-core model and the viscous flow around arbitrary bodies. The method solves for the flow field velocities on a body-fitted computational mesh using finite-difference techniques. The viscous flow field of the two-dimensional body is calculated on an Eulerian grid via the velocity/vorticity formulation of the Navier-Stokes equations.

The method demonstrates that the finite-core vortex model is accurate in convecting the interacting vortex wake away from the body. This will significantly reduce the need for a fine computational mesh away from the body to resolve the interacting vortex wake. Near the body, the interacting vortex wake is distributed to the computational mesh to provide accurate vortex interaction with the flow field.

A simulation of a rotor wake interaction with the flow about a circular cylinder and a 25% elliptic cylinder at 45 and 90 degrees incidence was shown for Reynolds number 3000. The simulation was considered to address the interaction of a rotor wake with the cross-section of the tail boom and empennage components. Results of the vortex interaction indicate that the presence of a interacting vortex wake has a profound effect on the flow field and therefore, the loading on the circular and elliptic cylinders. The calculation of vortex interactions with the flow about a circular and an elliptic cylinder were considered to evaluate general vortex interactions.

The lift and drag on the circular cylinder and the elliptic cylinder at 90 degrees incidence were significantly increased due to the interacting vortex wake. The lift on the circular cylinder during the interaction was increased significantly and the drag was slightly reduced from that for no interaction due to the effect of the interacting vortex wake on the circulation around the cylinder. The drag on the elliptic cylinder at 90 degrees incidence was significantly increased due to the vortex interaction. Spikes in the drag distribution, representing the passage of the vortices in the interacting vortex wake were shown. The magnitude of these spikes are significant with respect to the drag rise due to the vortex interaction.

Large variations in the loading of the elliptic cylinder at 45 degrees incidence were shown for changes in the rotation direction of the vortices in the interacting vortex wake. When the vortices were rotating in a clockwise direction, the lift and drag on the elliptic cylinder were significantly reduced during the vortex interaction. Conversely, when the vortices were rotating in a counter-clockwise direction, the lift and drag on the elliptic cylinder were significantly increased during the vortex interaction. These variations are important in understanding the interaction of the rotor wake with the flow about empennage components.

The present two-dimensional method has demonstrated the ability to efficiently compute the two-dimensional interaction of finite-core vortex wakes with the flow

about arbitrary bodies. The method is currently being extended to three-dimensional analysis.

References

1. Srinivasan, G.R., McCroskey, W.J., and Baeder, J.D., "Aerodynamics of Two-Dimensional Blade-Vortex Interaction," AIAA Journal, Vol. 24, No. 10, Oct. 1986, pp. 1569-1576.

2. Rai, M.M., "Navier-Stokes Simulations of Blade-Vortex Interaction Using High-Order Accurate Upwind Schemes," AIAA Paper 87-0543, Reno, NV, 1987.

3. Sheridan P.F. and Smith R.P., "Interactional Aerodynamics - A New Challenge for Helicopter Technology," 35th Annual National Forum of the American Helicopter Society, Washington, DC, May 1979.

4. Stremel P.M., "A Method for Modeling Finite Core Vortices in Wake Flow Calculations," AIAA Paper 84-0417, Reno, NV, 1984.

5. Stremel, P.M., "Aerodynamic Interaction Between Vortical Wakes and the Viscous Flow about a Circular Cylinder," AIAA Paper 85-4063, Colorado Springs, CO, 1985.

6. Cordova, J.Q. and Barth, T.J., "Grid Generation for General 2-D Regions Using Hyperbolic Equations," AIAA Paper 88-0520, Jan. 1988.

7. Peaceman, D.W. and Rachford, H. H., Jr., "The Numerical Solution of Parabolic and Elliptic Differential Equations," Journal of the Society for Industrial Applied Mathematics, Vol. 3, No. 1, 1955, pp. 28-41.

8. Stremel P.M., "Aerodynamic Interaction Between Vortical Wakes and the Lifting Two-Dimensional Bodies," NASA TM-101074, March 1989.

9. Bouard, R. and Coutanceau, M., "The Early Stage of Development of the Wake behind an Impulsively Started Cylinder for $40 < R_e < 10^4$," Journal of Fluid Mechanics, Vol. 101, 1980, pp. 583.

10. Loc, Ta Phuoc and Bouard, R. "Numerical Solution of the Early Stage of the Unsteady Viscous Flow around a Circular Cylinder: A comparison with Experimental Visualization and Measurements," Journal of Fluid Mechanics, Vol. 160, 1985, pp. 93-117.

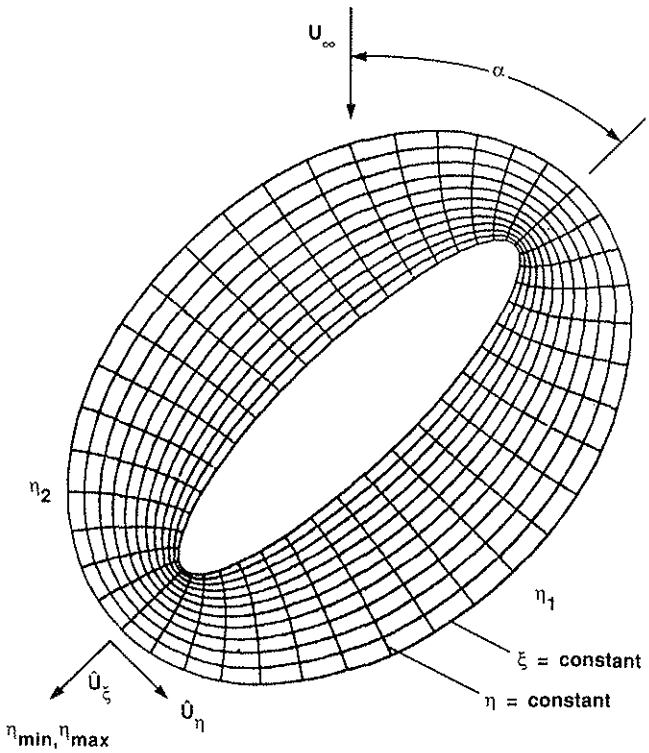

Fig 1 Computational geometry.

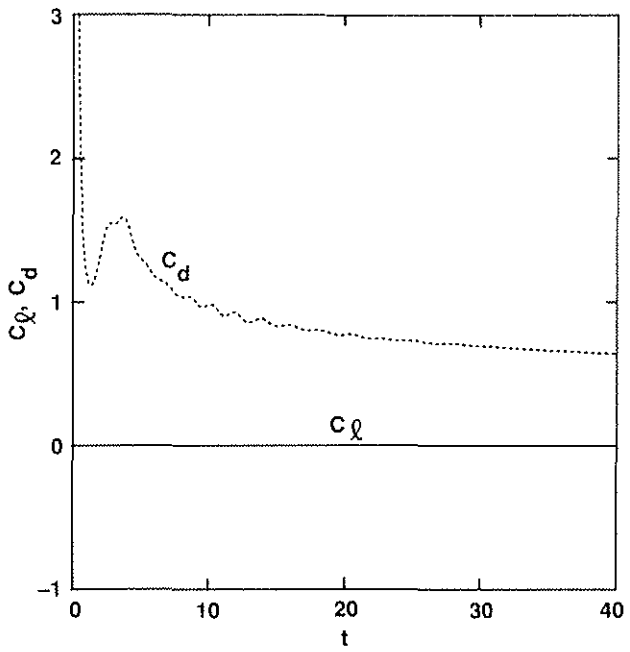

Fig 2 Lift and drag coefficients for circular cylinder, $R_e = 3000$, $\alpha = 0°$.

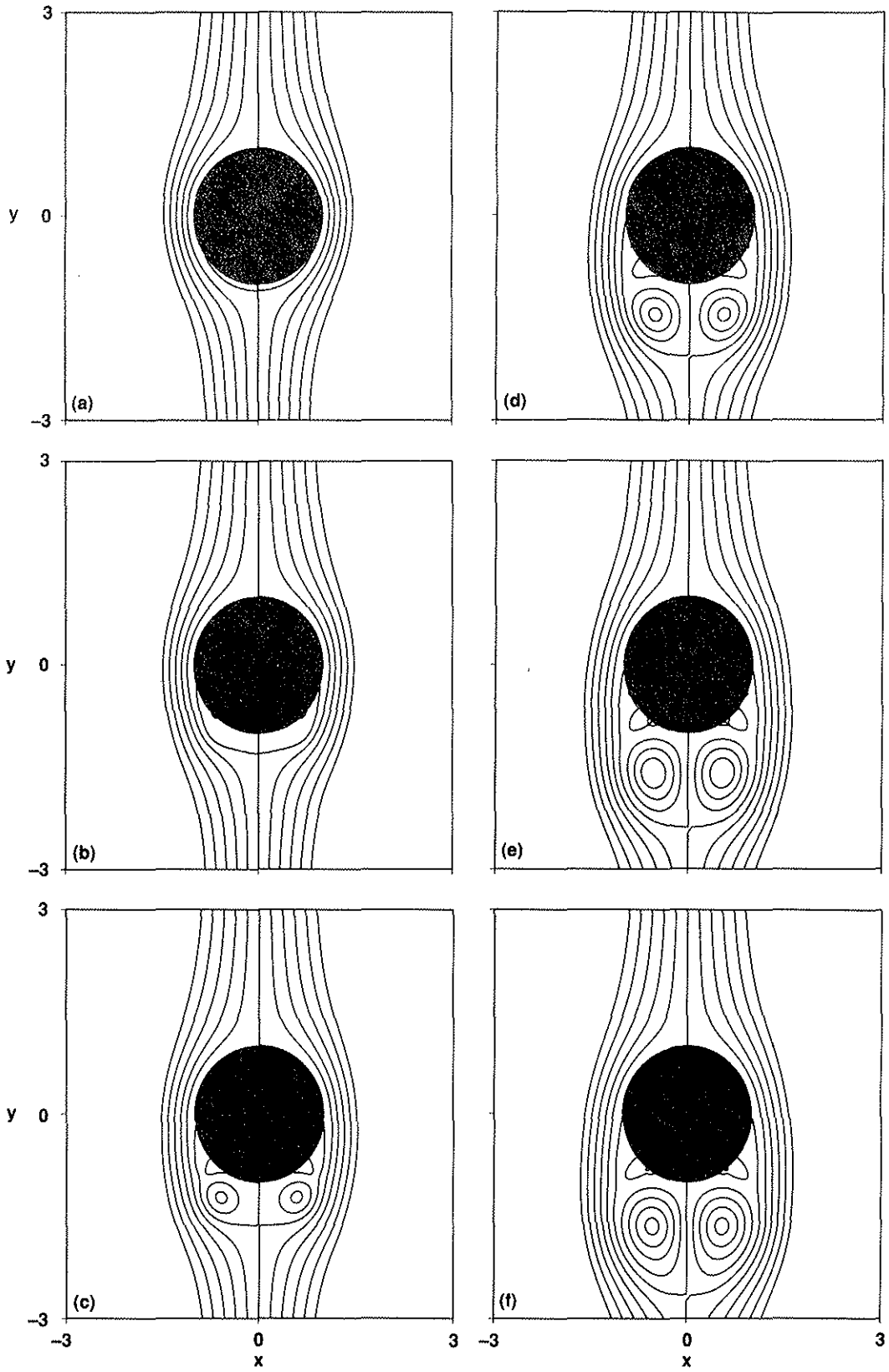

Fig 3 Streamline contours for circular cylinder, R_e = 3000, α = 0°. (a) t = 1.0, (b) t = 2.0, (c) t = 3.0, (d) t = 4.0, (e) t = 5.0, (f) t = 6.0.

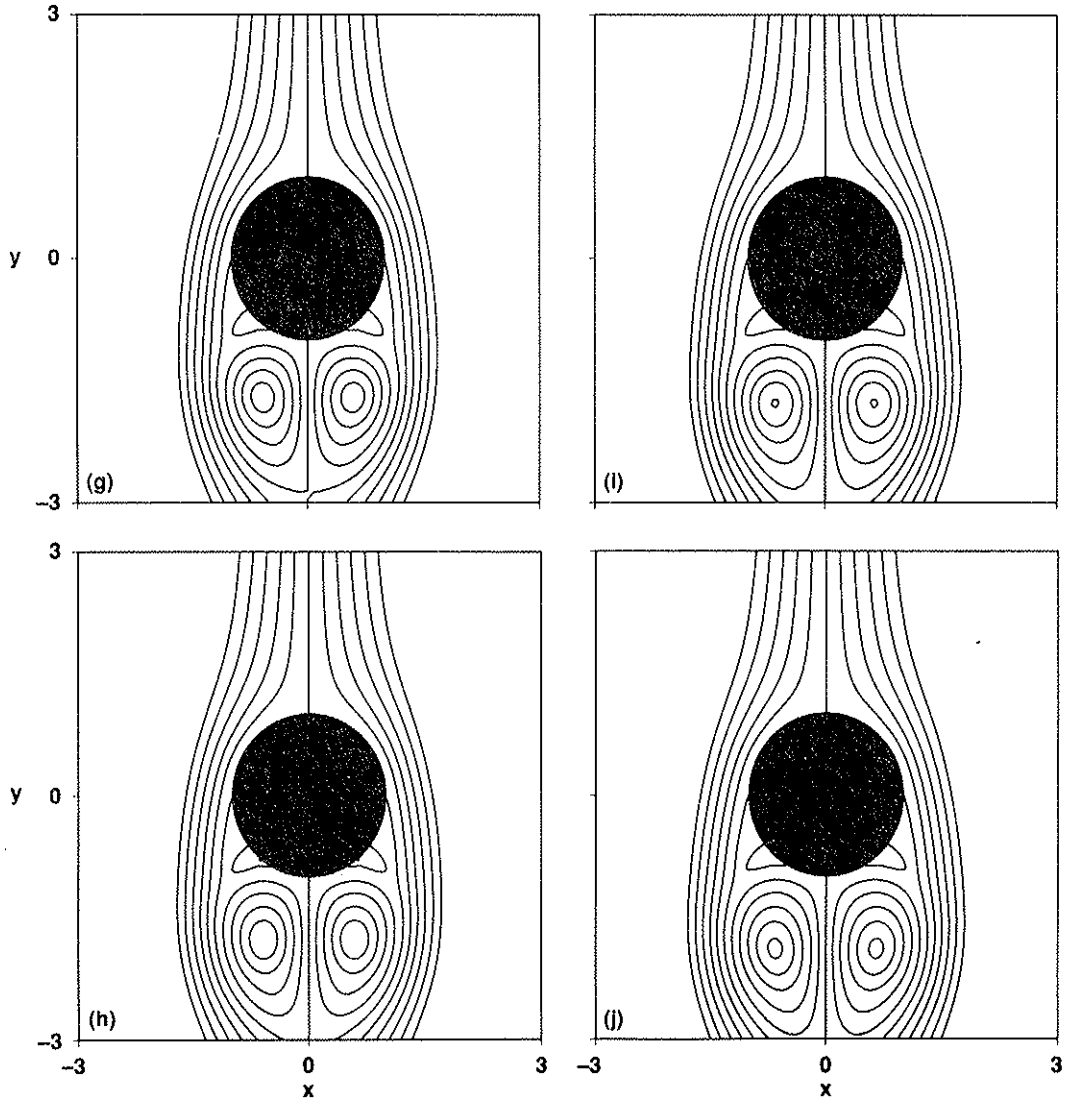

Fig 3 Concluded. (g) t = 7.0, (h) t = 8.0, (i) t = 9.0, (j) t = 10.0.

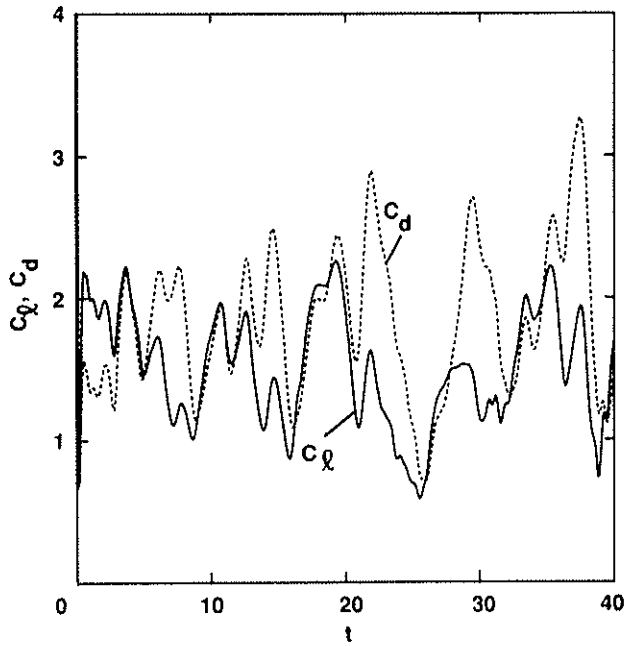

Fig 4 Lift and drag coefficients for an elliptic cylinder, $R_e = 3000$, $\alpha = 45°$.

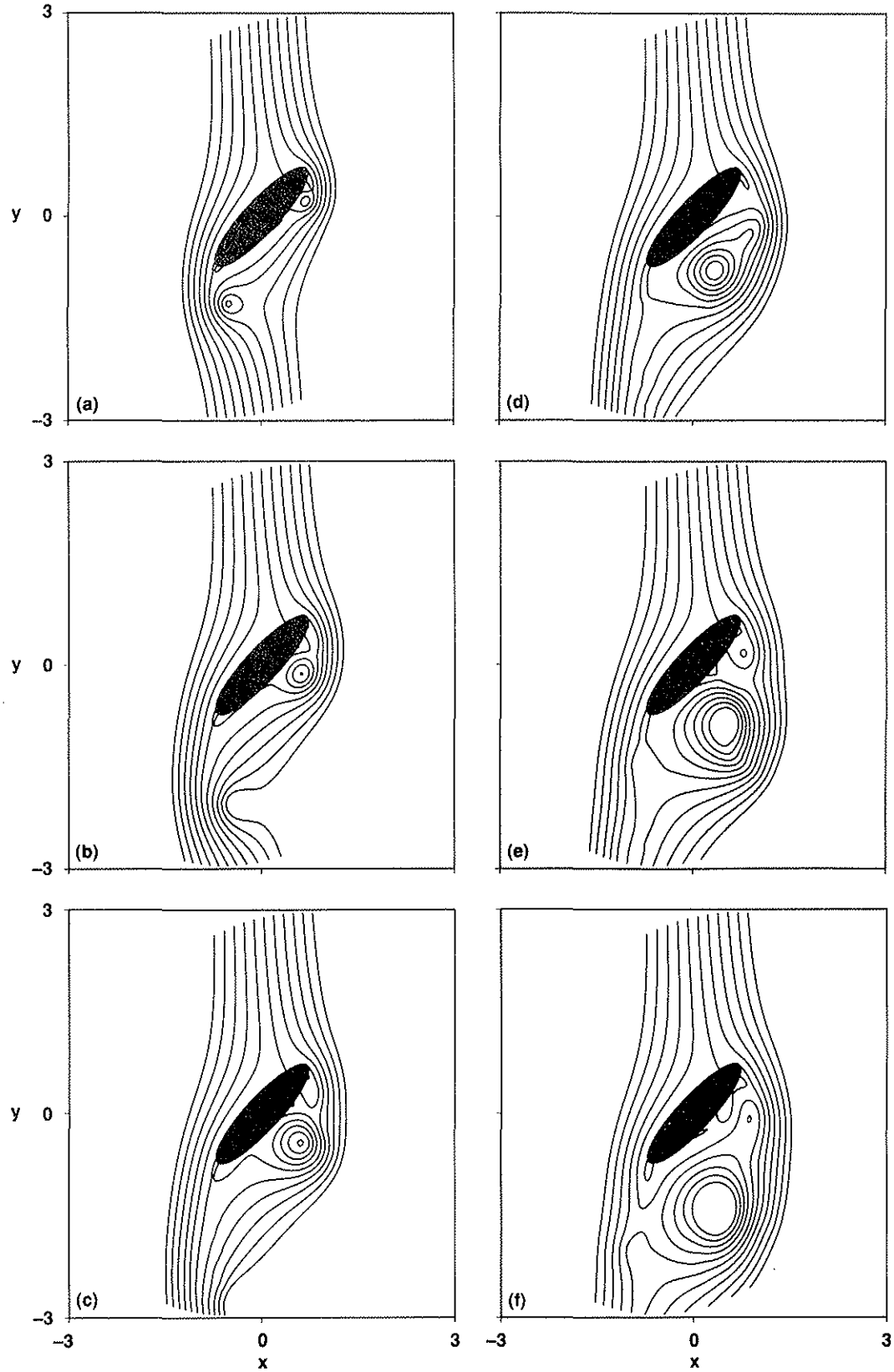

Fig 5 Streamline contours for an elliptic cylinder, R_e = 3000, α = 45°. (a) t = 1.0, (b) t = 2.0, (c) t = 3.0, (d) t = 4.0, (e) t = 5.0, (f) t = 6.0.

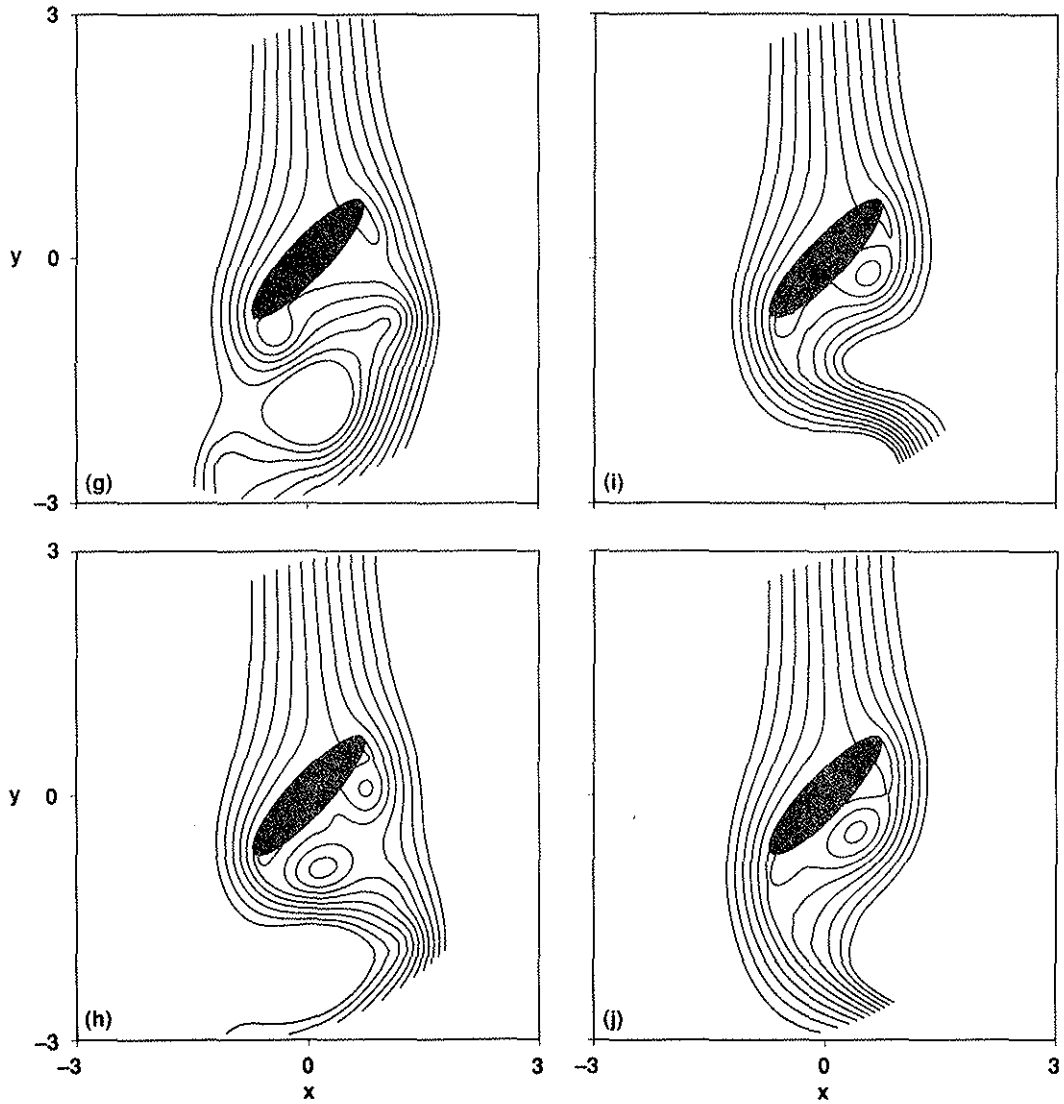

Fig 5 Concluded. (g) t = 7.0, (h) t = 8.0, (i) t = 9.0, (j) t = 10.0.

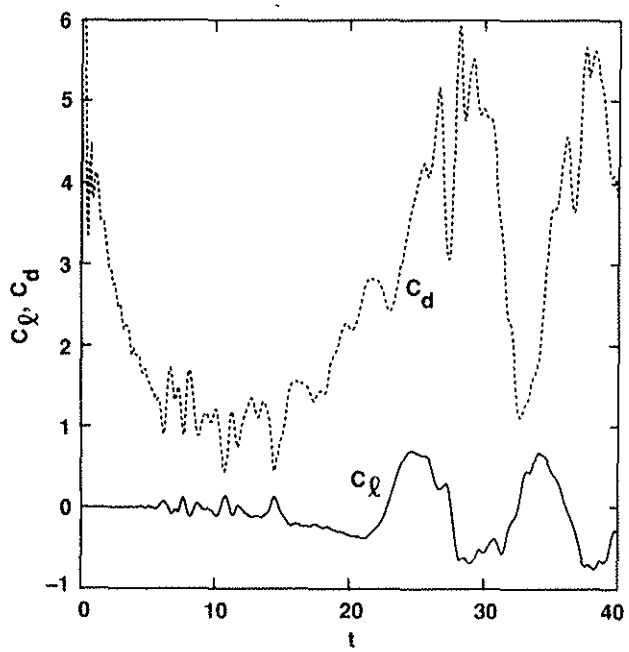

Fig 6 Lift and drag coefficients for an elliptic cylinder, $R_e = 3000$, $\alpha = 90°$.

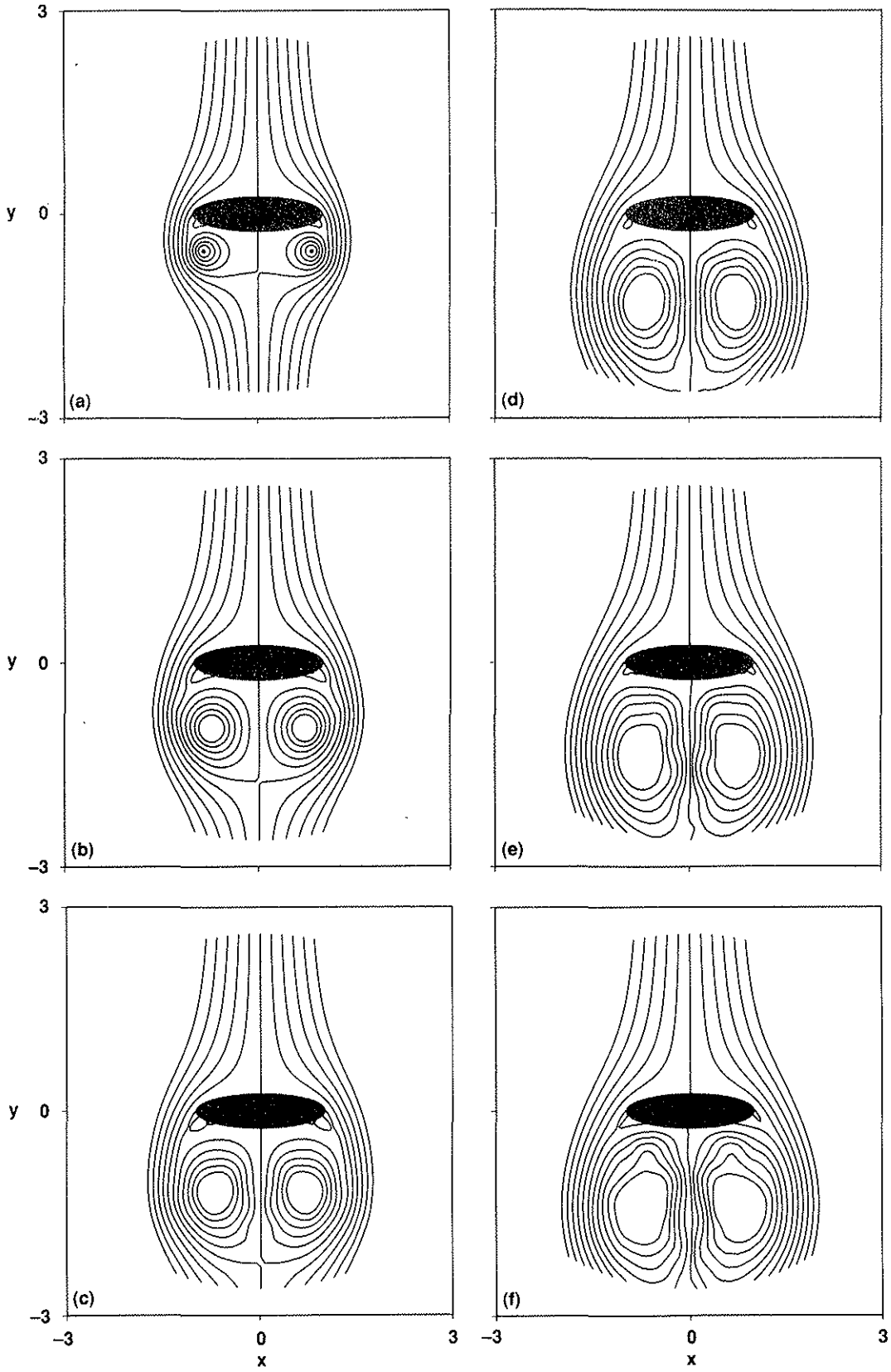

Fig 7 Streamline contours for an elliptic cylinder, $R_e = 3000$, $\alpha = 90°$. (a) t = 1.0, (b) t = 2.0, (c) t = 3.0, (d) t = 4.0, (e) t = 5.0, (f) t = 6.0.

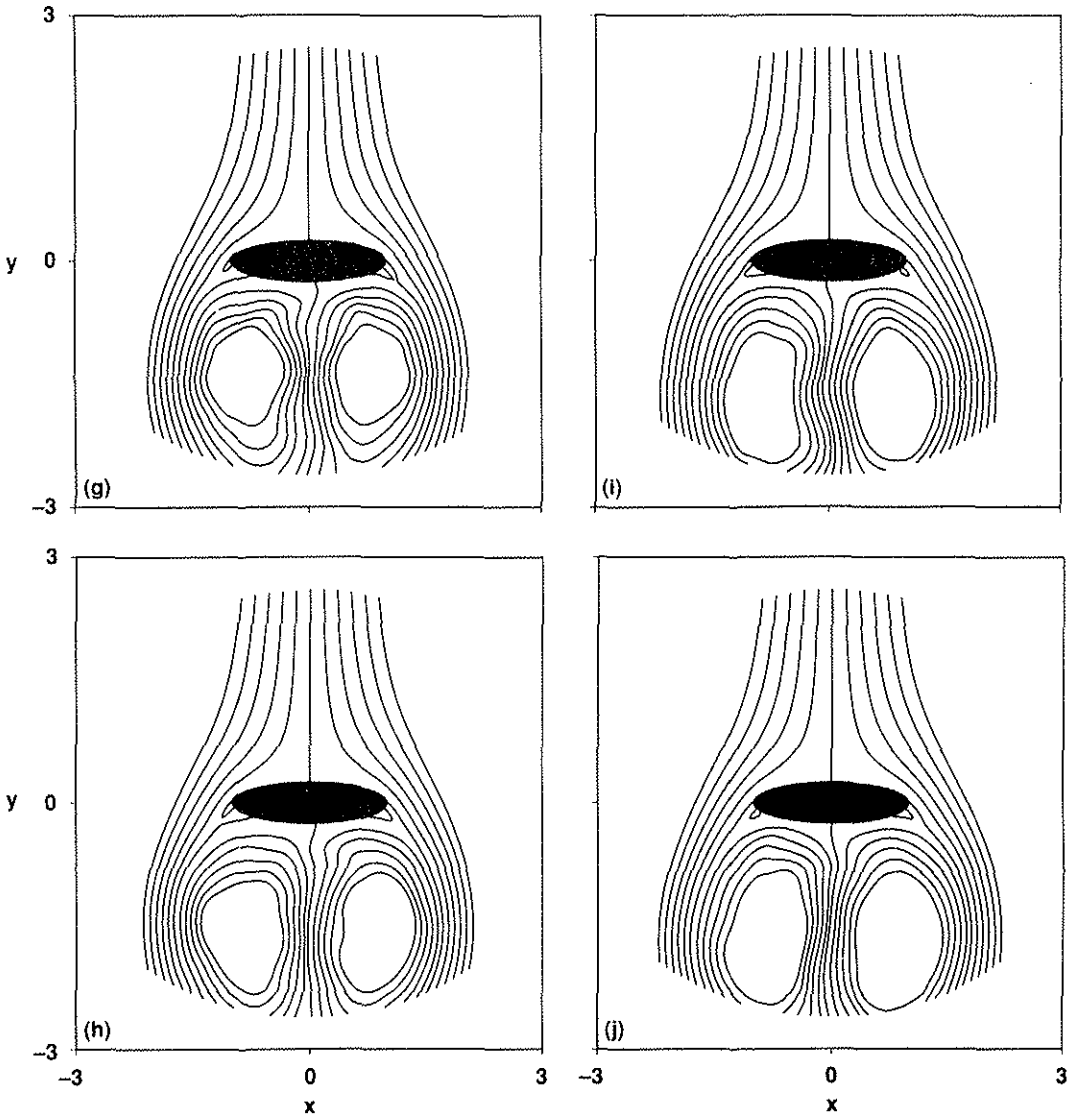

Fig 7 Concluded. (g) t = 7.0, (h) t = 8.0, (i) t = 9.0, (j) t = 10.0.

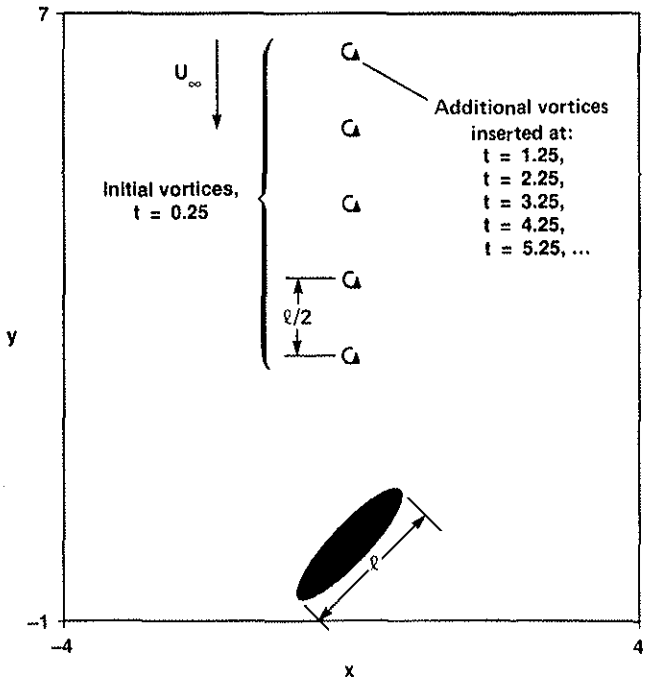

Fig 8 - Schematic of vortex interaction.

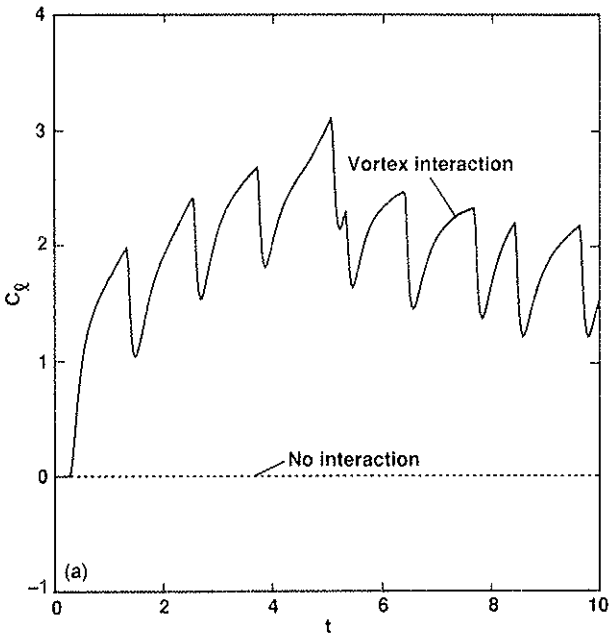

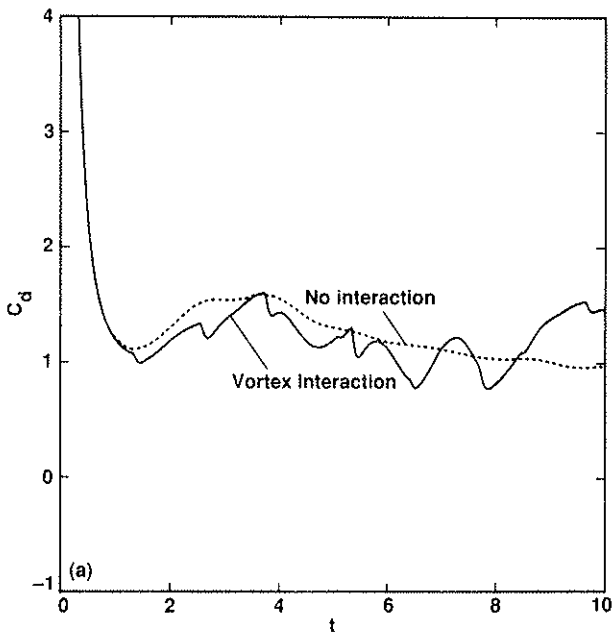

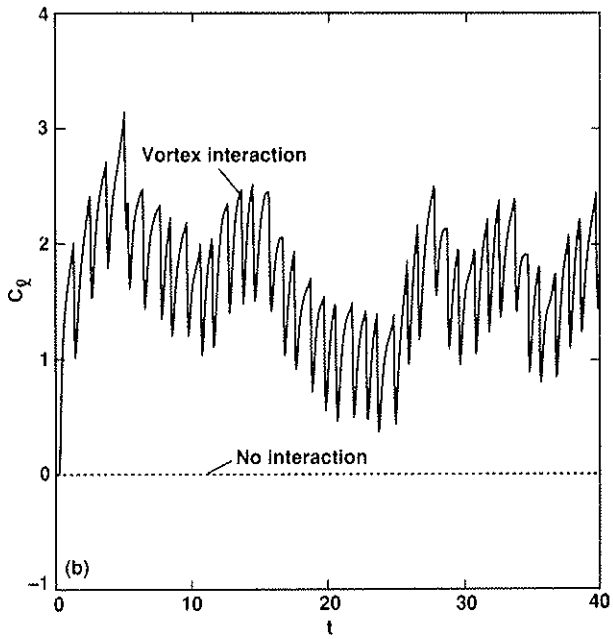

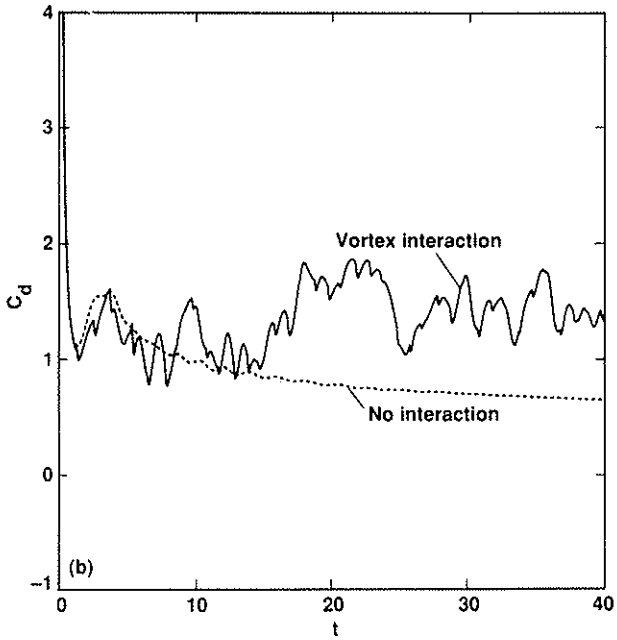

Fig 9 Lift coefficient for vortex interaction of vortex strength $\Gamma = 1.0$, $r_o = 0.1$, circular cylinder, $R_e = 3000$, $\alpha = 0°$. (a) $t \leq 10.0$, (b) $t \leq 40.0$.

Fig 10 Drag coefficient for vortex interaction of vortex strength $\Gamma = 1.0$, $r_o = 0.1$, circular cylinder, $R_e = 3000$, $\alpha = 0°$. (a) $t \leq 10.0$, (b) $t \leq 40.0$.

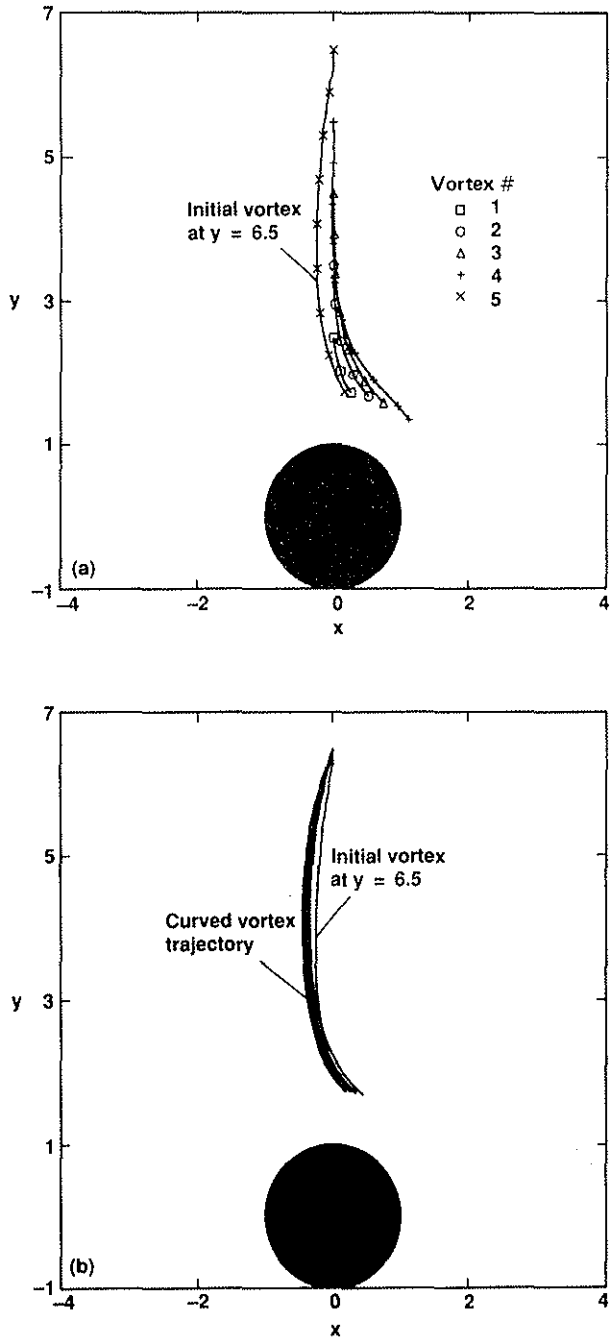

Fig 11 Vortex trajectories for vortex interaction of vortex strength $\Gamma = 1.0$, $r_o = 0.1$, circular cylinder, $R_e = 3000$, $\alpha = 0°$. (a) initial vortices, $t = 0.25$, (b) additional vortices, $\Delta t = 1.0$.

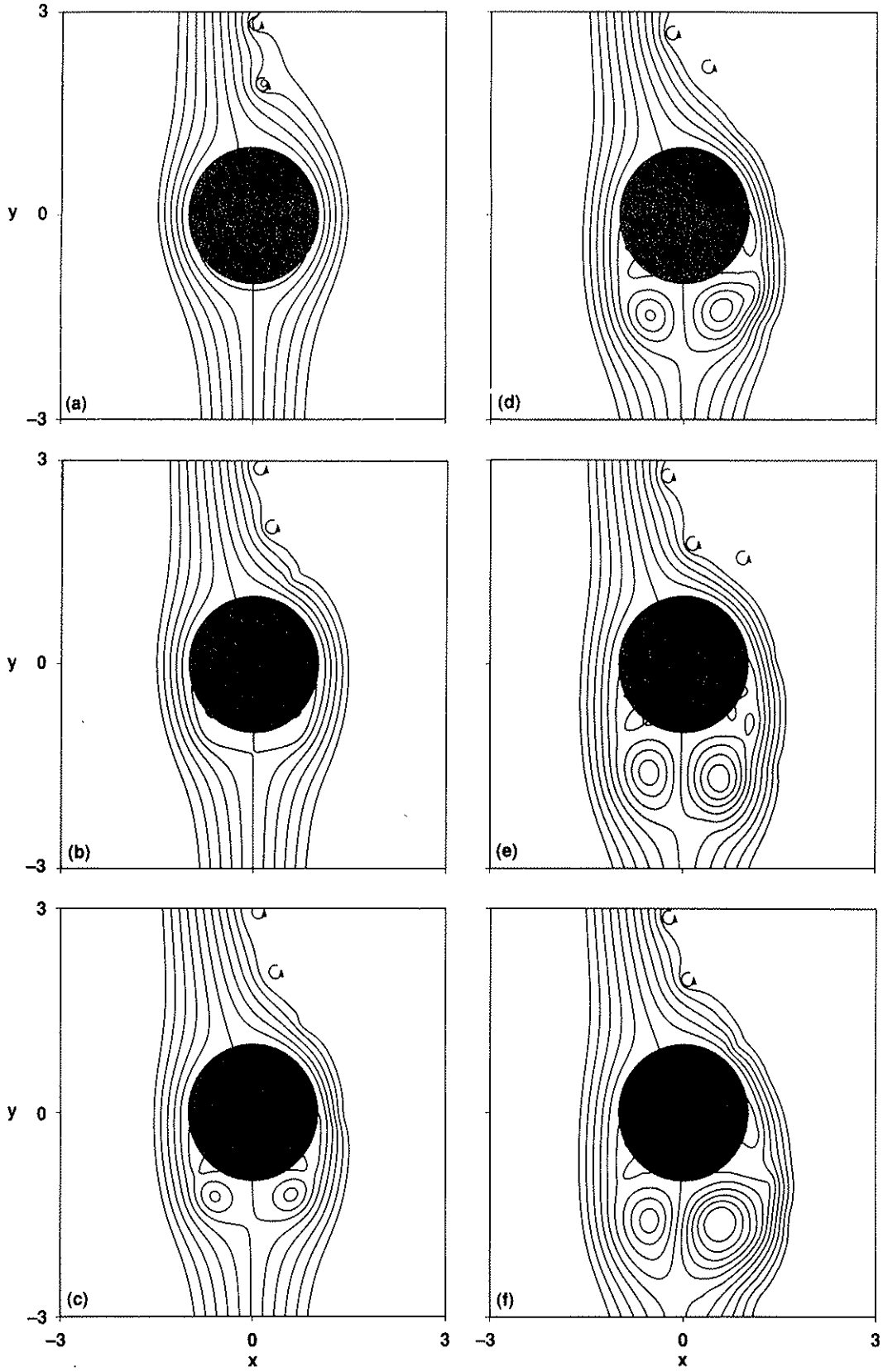

Fig 12 Streamline contours for vortex interaction of vortex strength $\Gamma = 1.0$, $r_0 = 0.1$, circular cylinder, $R_e = 3000$, $\alpha = 0°$. (a) t = 1.0, (b) t = 2.0, (c) t = 3.0, (d) t = 4.0, (e) t = 5.0, (f) t = 6.0.

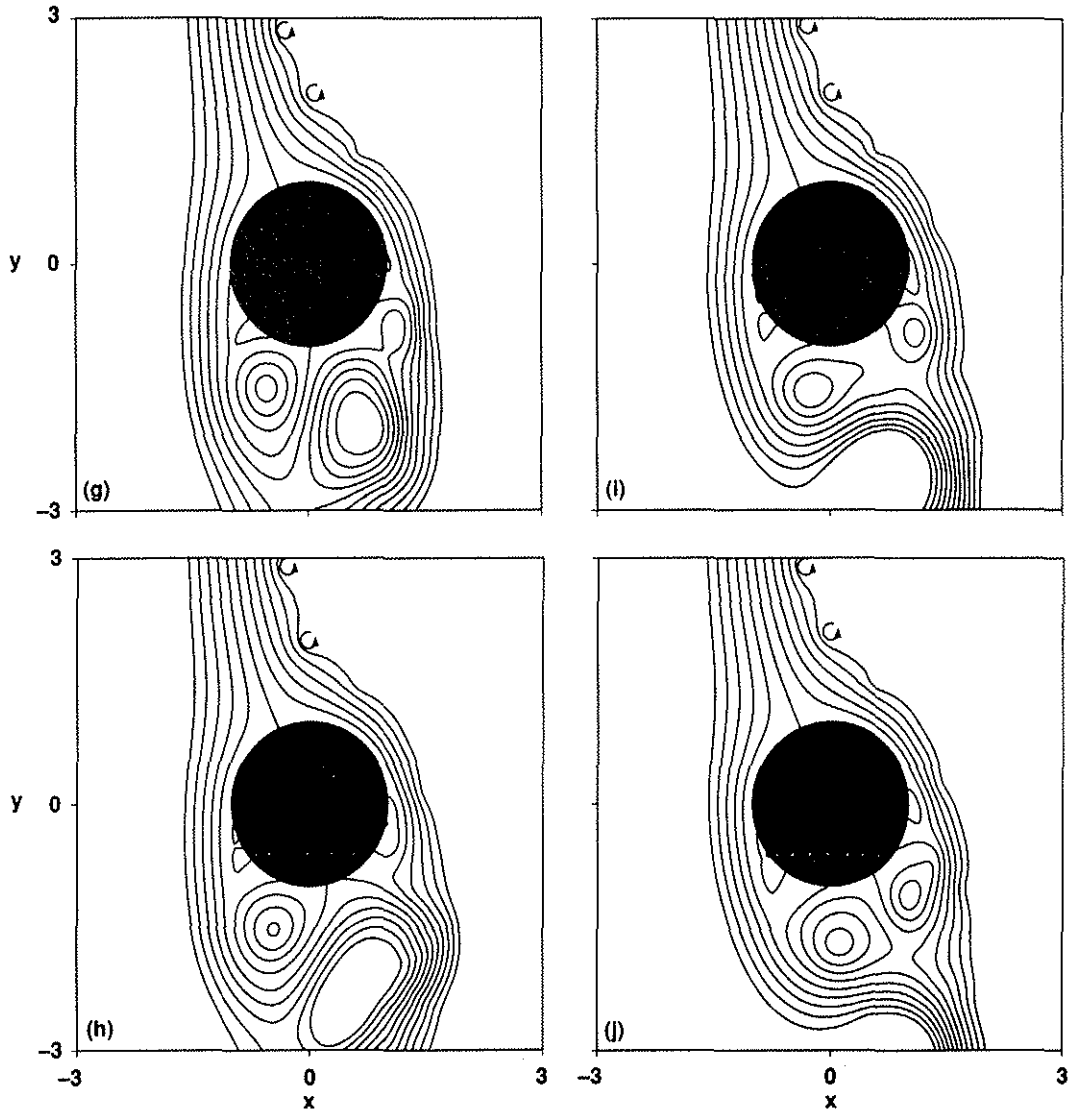

Fig 12 Concluded. (g) t = 7.0, (h) t = 8.0, (i) t = 9.0, (j) t = 10.0.

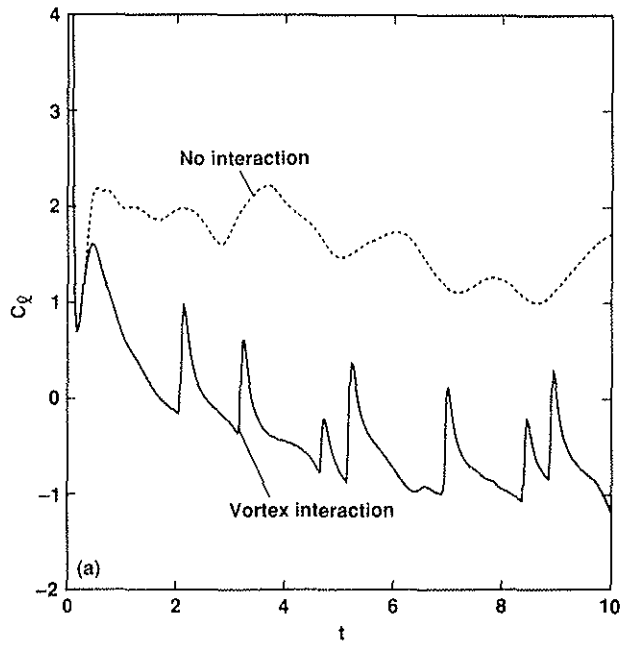

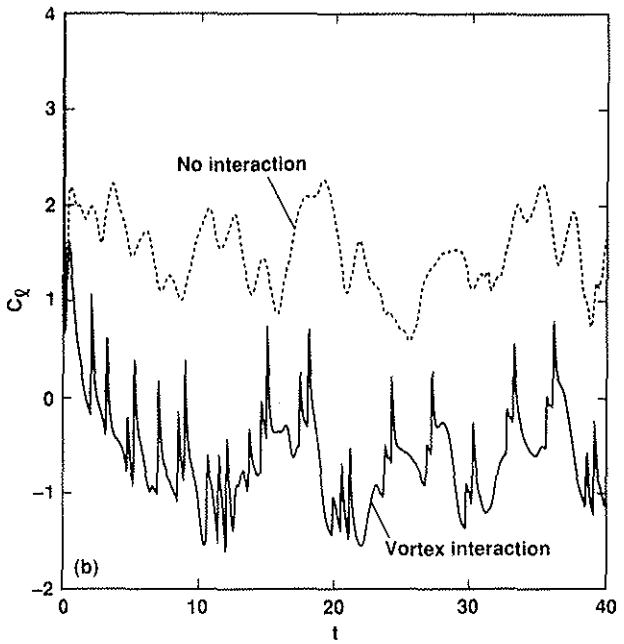

Fig 13 Lift coefficient for vortex interaction of vortex strength $\Gamma = -1.0$, $r_o = 0.1$, elliptic cylinder, $R_e = 3000$, $\alpha = 45°$. (a) $t \leq 10.0$, (b) $t \leq 40.0$.

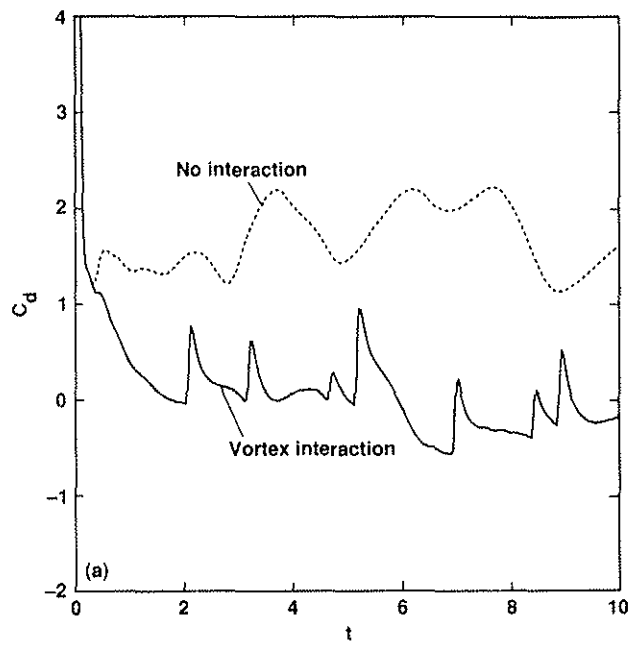

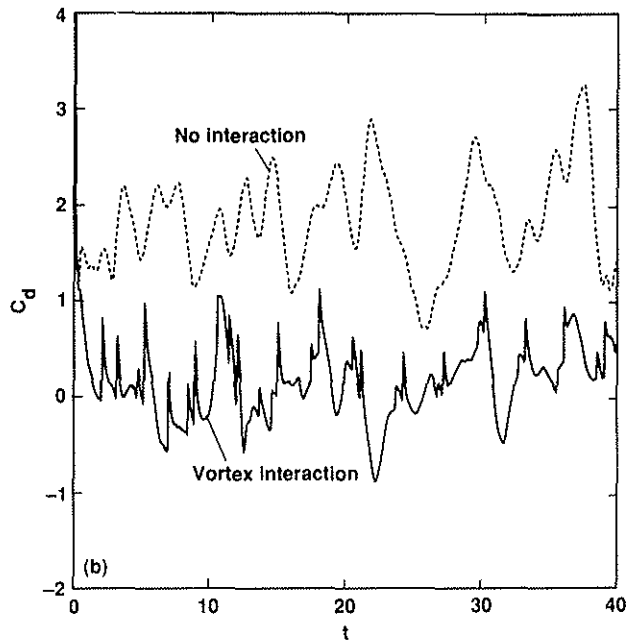

Fig 14 Drag coefficient for vortex interaction of vortex strength $\Gamma = -1.0$, $r_o = 0.1$, elliptic cylinder, $Re = 3000$, $\alpha = 45°$. (a) $t \leq 10.0$, (b) $t \leq 40.0$.

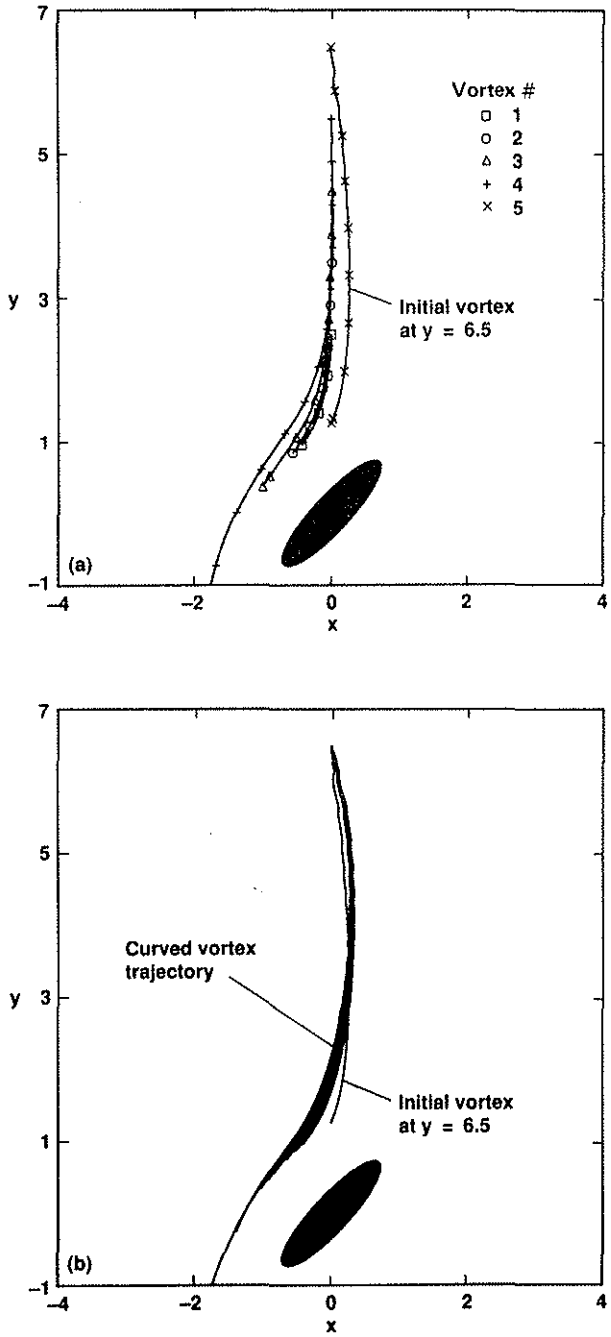

Fig 15 Vortex trajectories for vortex interaction of vortex strength $\Gamma = -1.0$, $r_0 = 0.1$, elliptic cylinder, Re = 3000, $\alpha = 45°$. (a) initial vortices, t = 0.25, (b) additional vortices, $\Delta t = 1.0$.

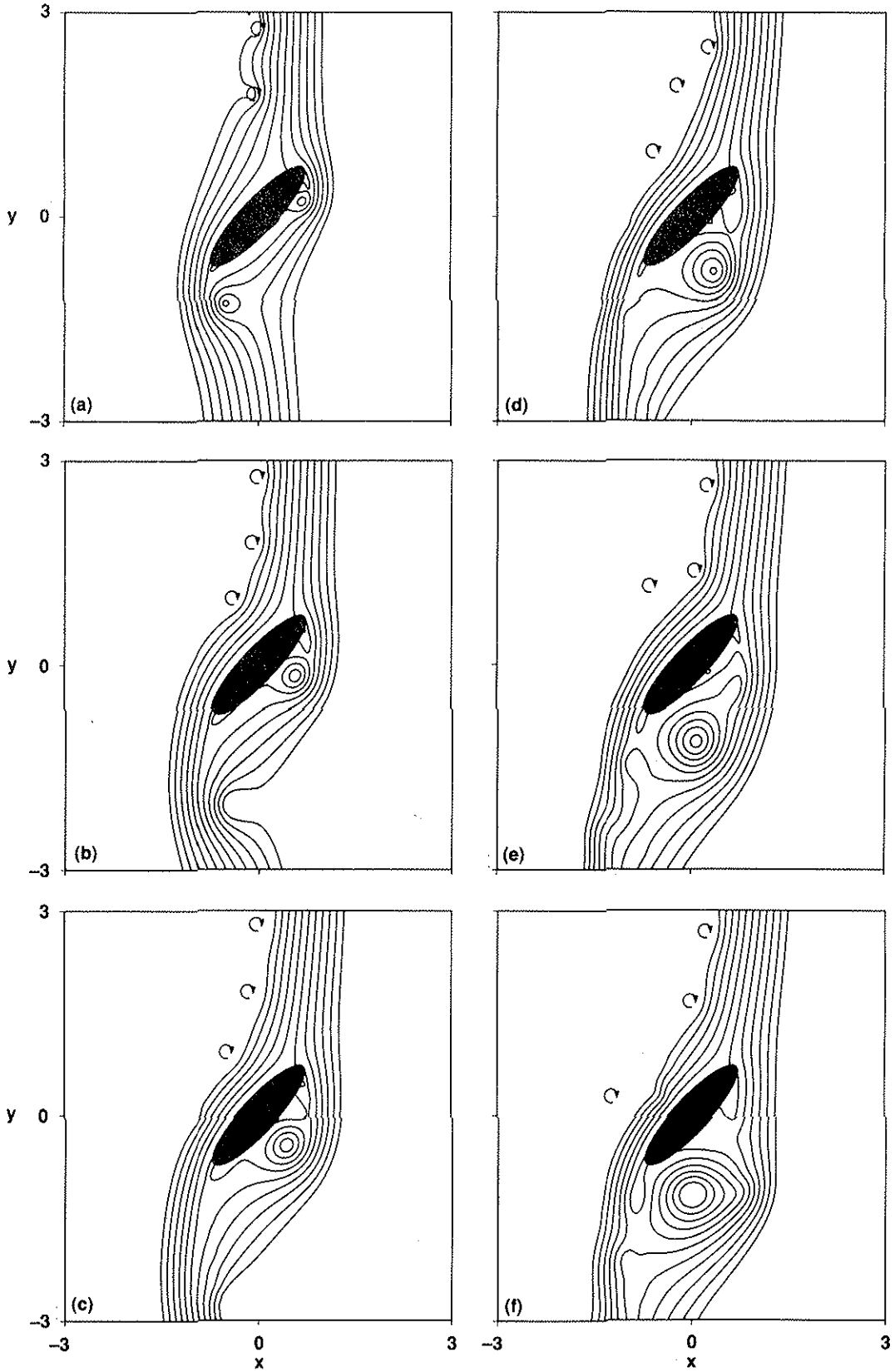

Fig 16 Streamline contours for vortex interaction of vortex strength $\Gamma = -1.0$, $r_O = 0.1$, elliptic cylinder, $R_e = 3000$, $\alpha = 45°$. (a) t = 1.0, (b) t = 2.0, (c) t = 3.0, (d) t = 4.0, (e) t = 5.0, (f) t = 6.0.

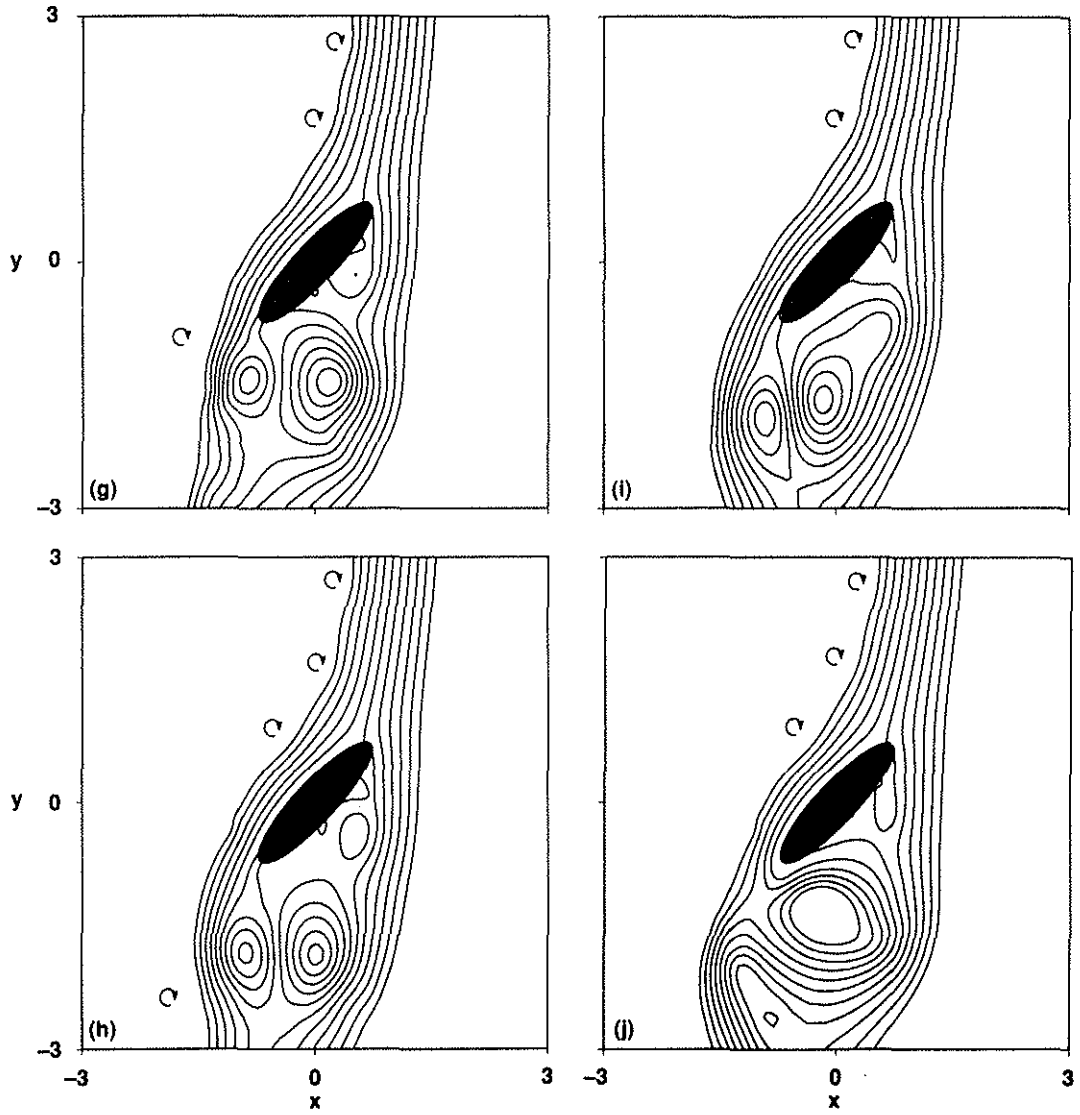

Fig 16 Concluded. (g) t = 7.0, (h) t = 8.0, (i) t = 9.0, (j) t = 10.0.

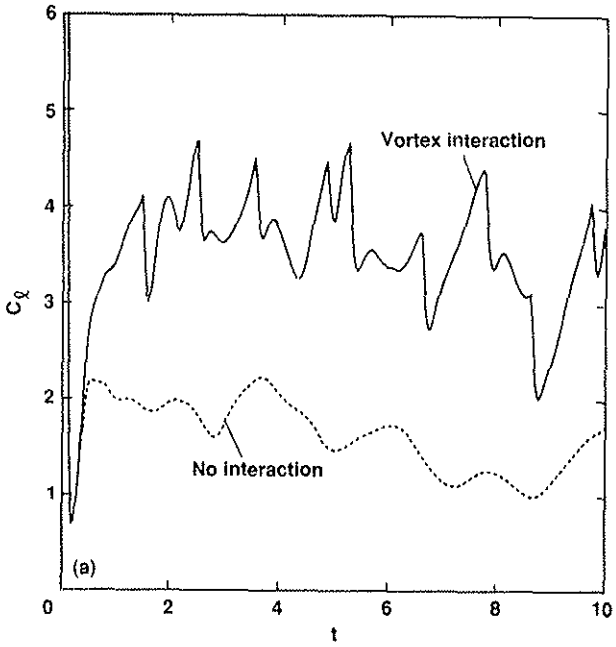

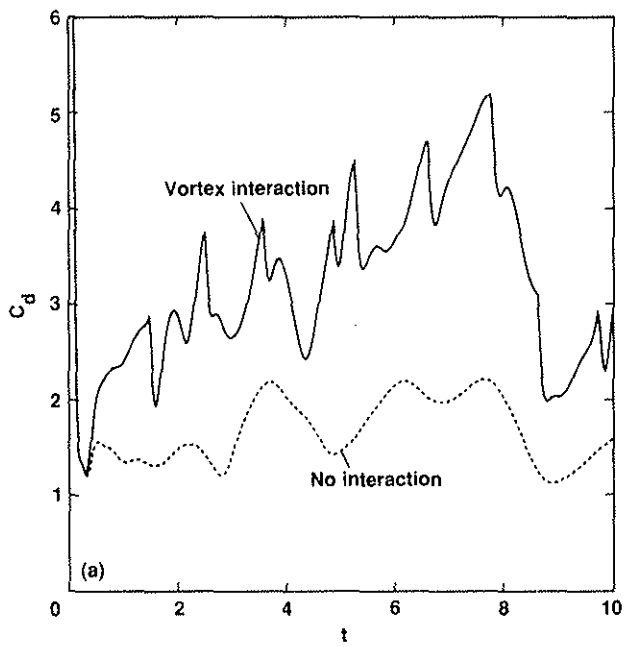

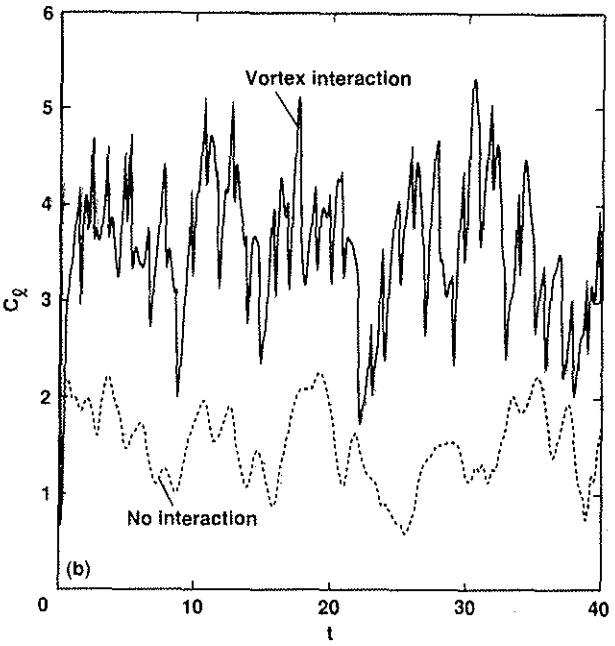

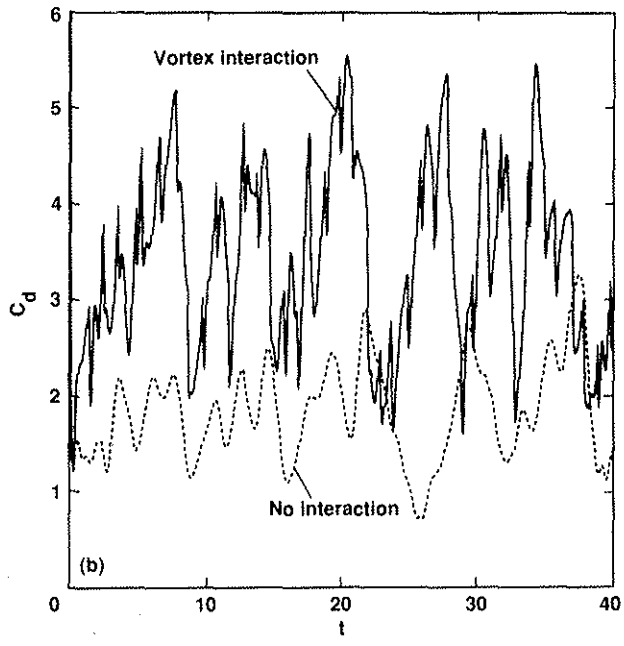

Fig 17 Lift coefficient for vortex interaction of vortex strength $\Gamma = 1.0$, $r_o = 0.1$, elliptic cylinder, $R_e = 3000$, $\alpha = 45°$. (a) $t \leq 10.0$, (b) $t \leq 40.0$.

Fig 18 Drag coefficient for vortex interaction of vortex strength $\Gamma = 1.0$, $r_o = 0.1$, elliptic cylinder, $Re = 3000$, $\alpha = 45°$. (a) $t \leq 10.0$, (b) $t \leq 40.0$.

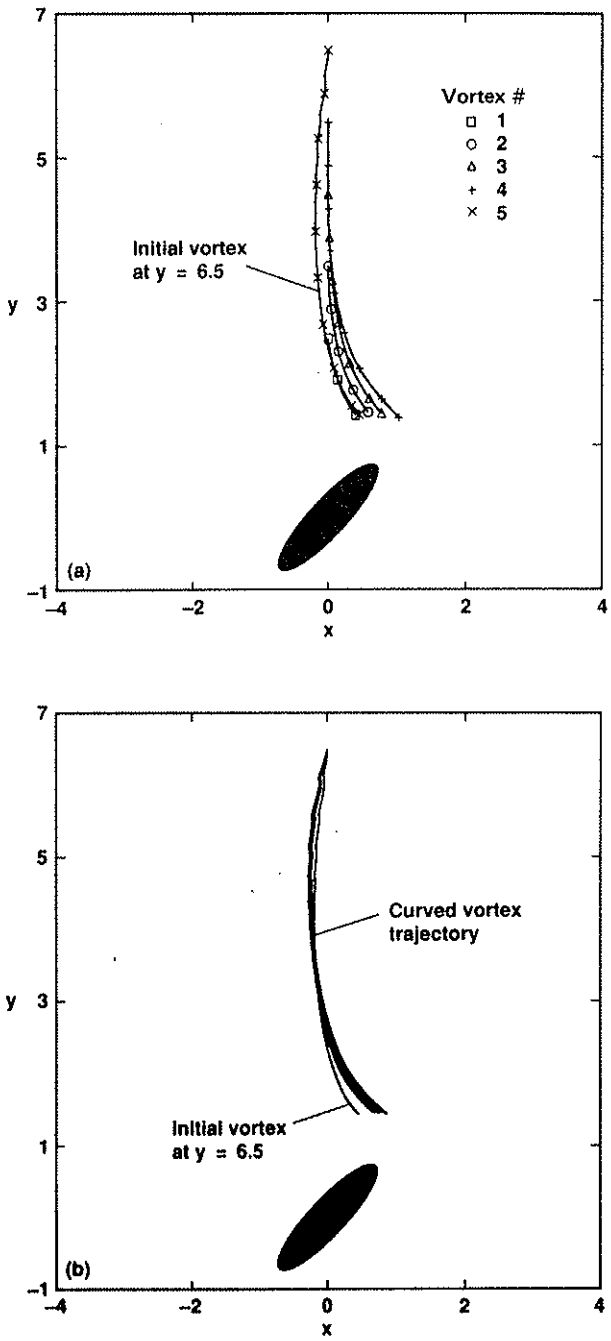

Fig 19 Vortex trajectories for vortex interaction of vortex strength $\Gamma = 1.0$, $r_0 = 0.1$, elliptic cylinder, Re = 3000, $\alpha = 45°$. (a) initial vortices, t = 0.25 (b) additional vortices, $\Delta t = 1.0$.

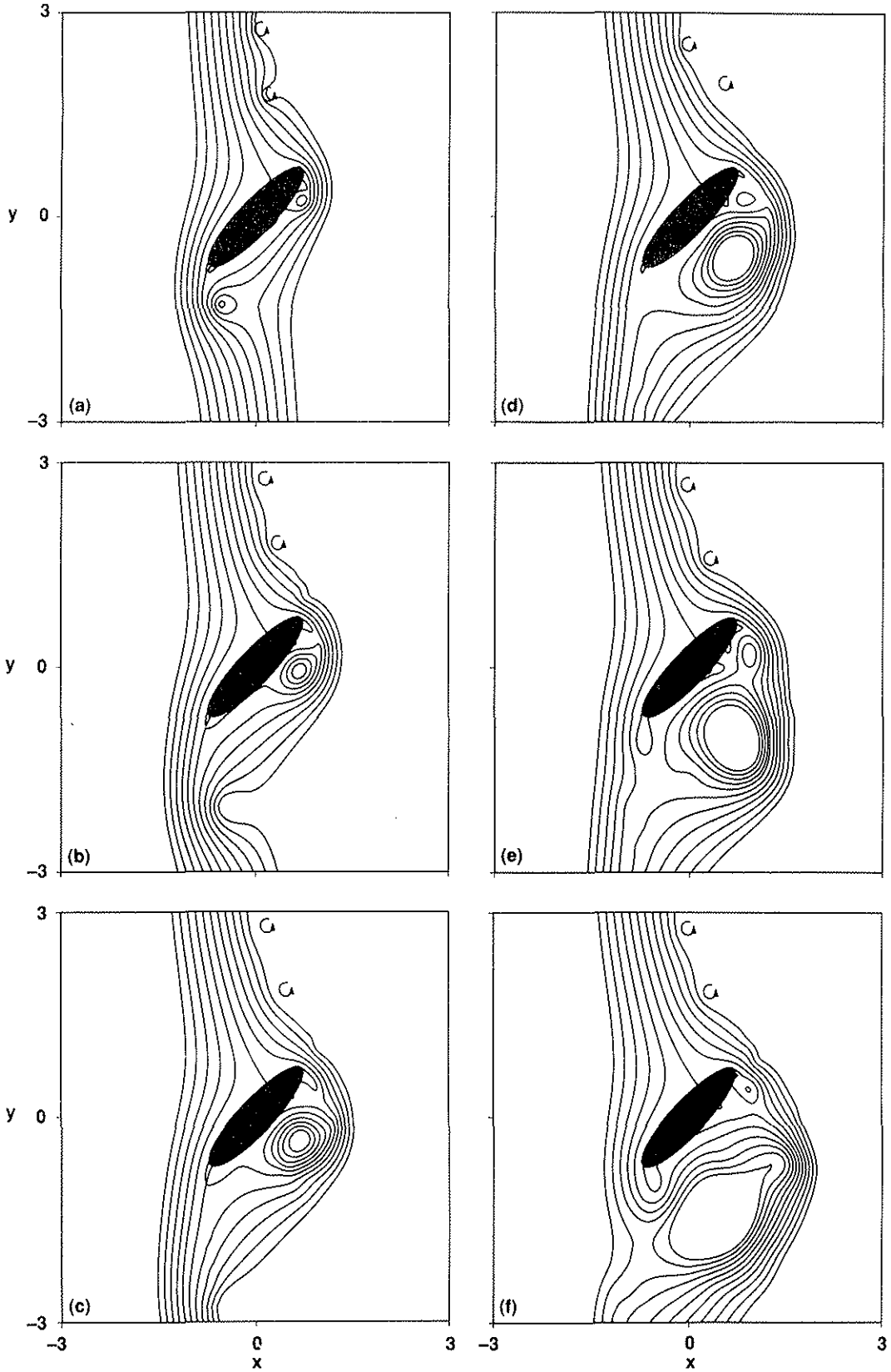

Fig 20 Streamline contours for vortex interaction of vortex strength $\Gamma = 1.0$, $r_o = 0.1$, elliptic cylinder, $R_e = 3000$, $\alpha = 45°$. (a) t = 1.0, (b) t = 2.0, (c) t = 3.0, (d) t = 4.0, (e) t = 5.0, (f) t = 6.0.

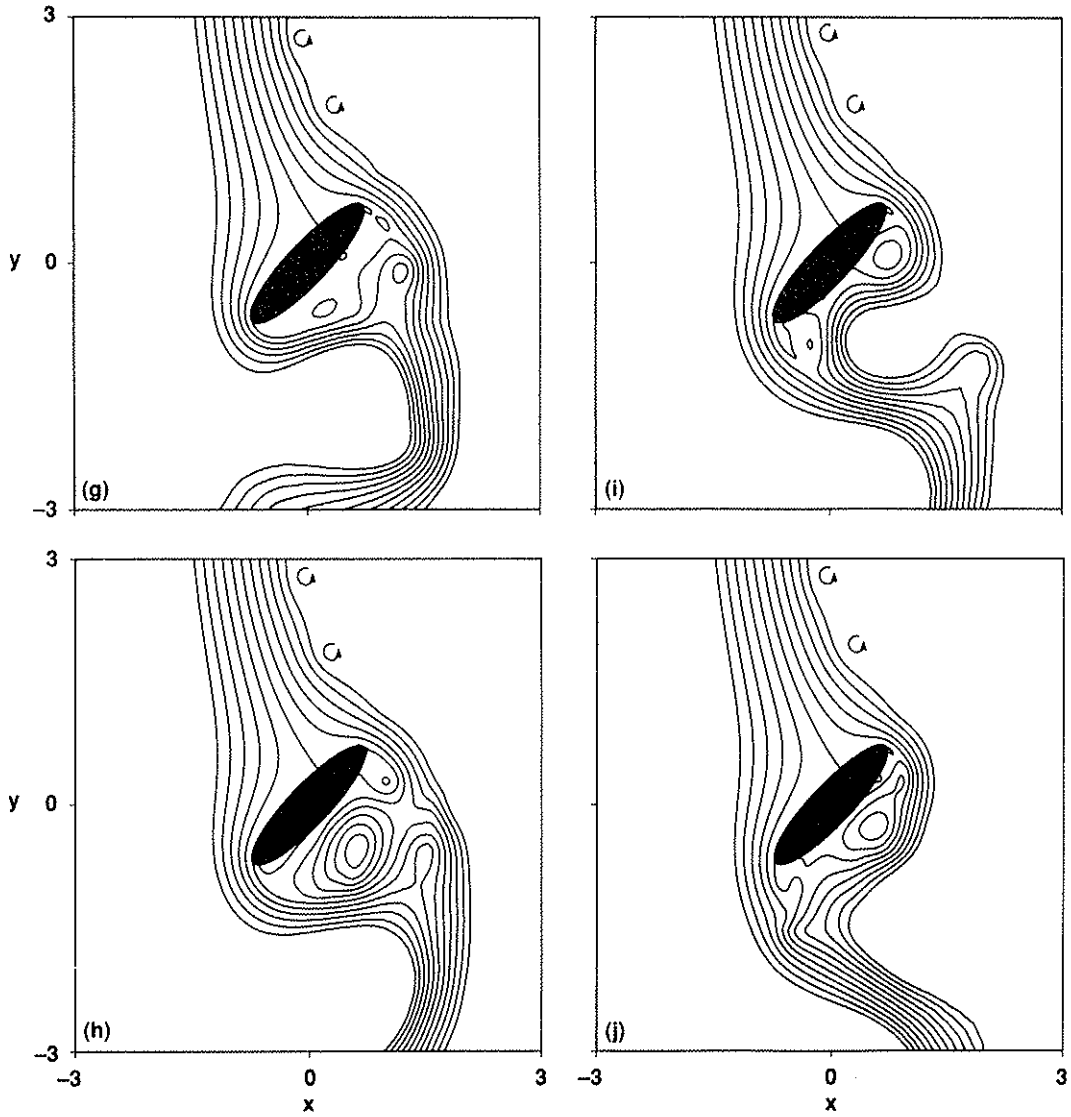

Fig 20 Concluded. (g) t = 7.0, (h) t = 8.0, (i) t = 9.0, (j) t = 10.0.

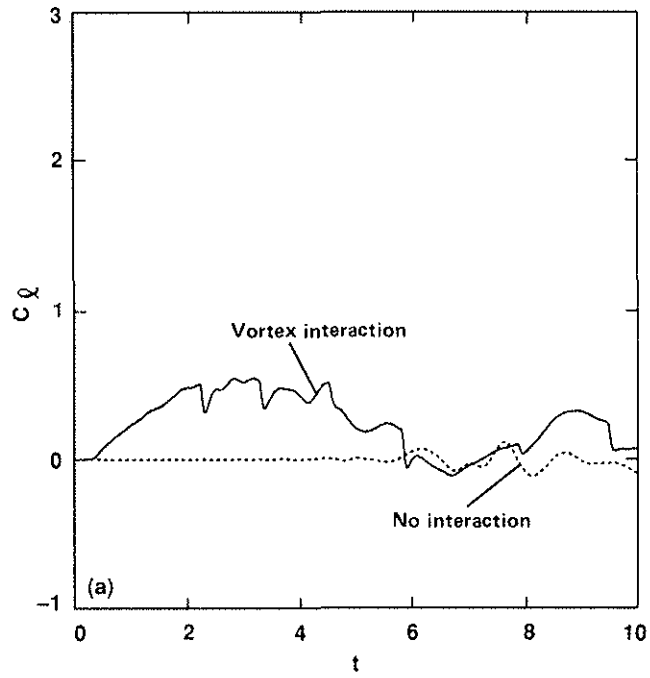

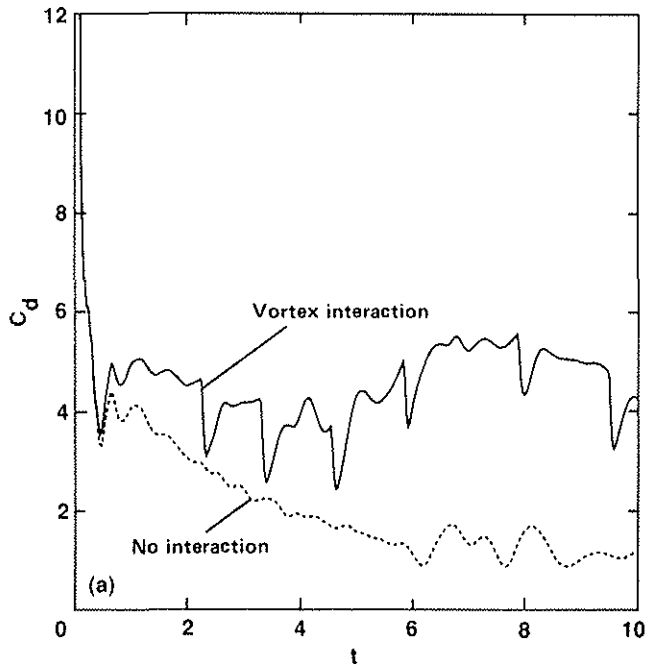

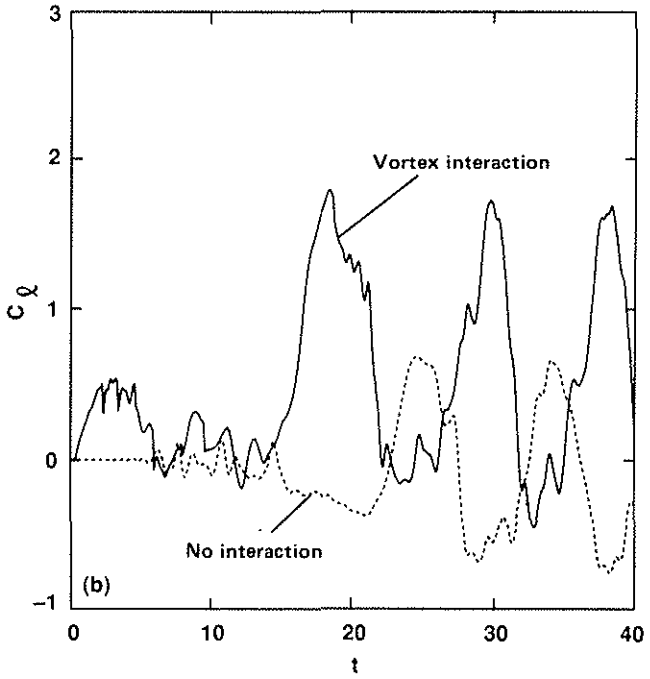

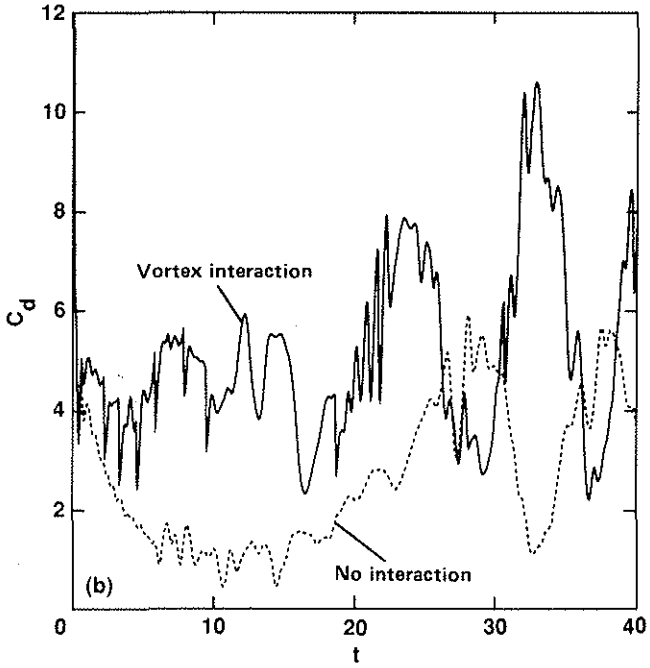

Fig 21 Lift coefficient for vortex interaction of vortex strength $\Gamma = 1.0$, $r_o = 0.1$, elliptic cylinder, $R_e = 3000$, $\alpha = 90°$. (a) $t \leq 10.0$, (b) $t \leq 40.0$.

Fig 22 Drag coefficient for vortex interaction of vortex strength $\Gamma = 1.0$, $r_o = 0.1$, elliptic cylinder, $Re = 3000$, $\alpha = 90°$. (a) $t \leq 10.0$, (b) $t \leq 40.0$.

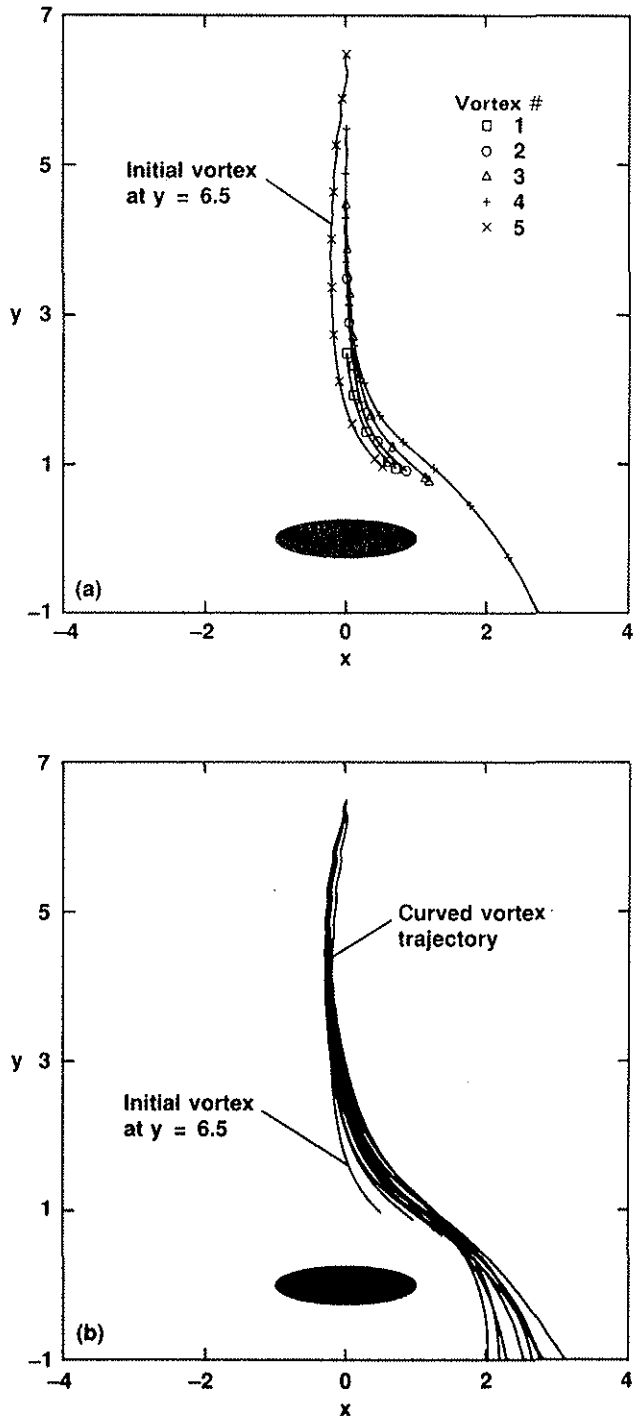

Fig 23 Vortex trajectories for vortex interaction of vortex strength $\Gamma = 1.0$, $r_0 = 0.1$, elliptic cylinder, Re = 3000, $\alpha = 90°$. (a) initial vortices, t = 0.25, (b) additional vortices, $\Delta t = 1.0$.

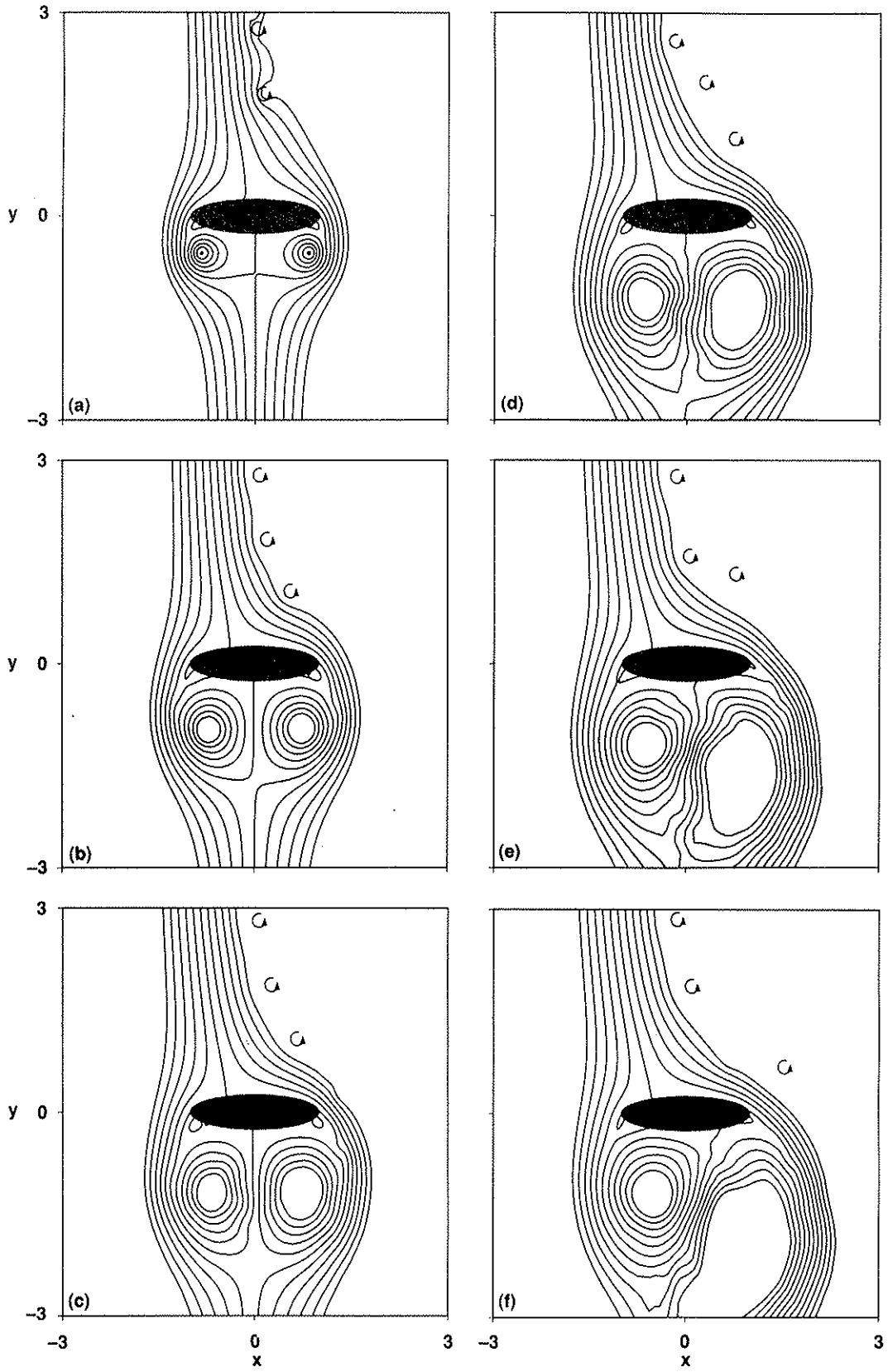

Fig 24 Streamline contours for vortex interaction of vortex strength $\Gamma = 1.0$, $r_o = 0.1$, elliptic cylinder, $R_e = 3000$, $\alpha = 90°$. (a) t = 1.0, (b) t = 2.0, (c) t = 3.0, (d) t = 4.0, (e) t = 5.0, (f) t = 6.0.

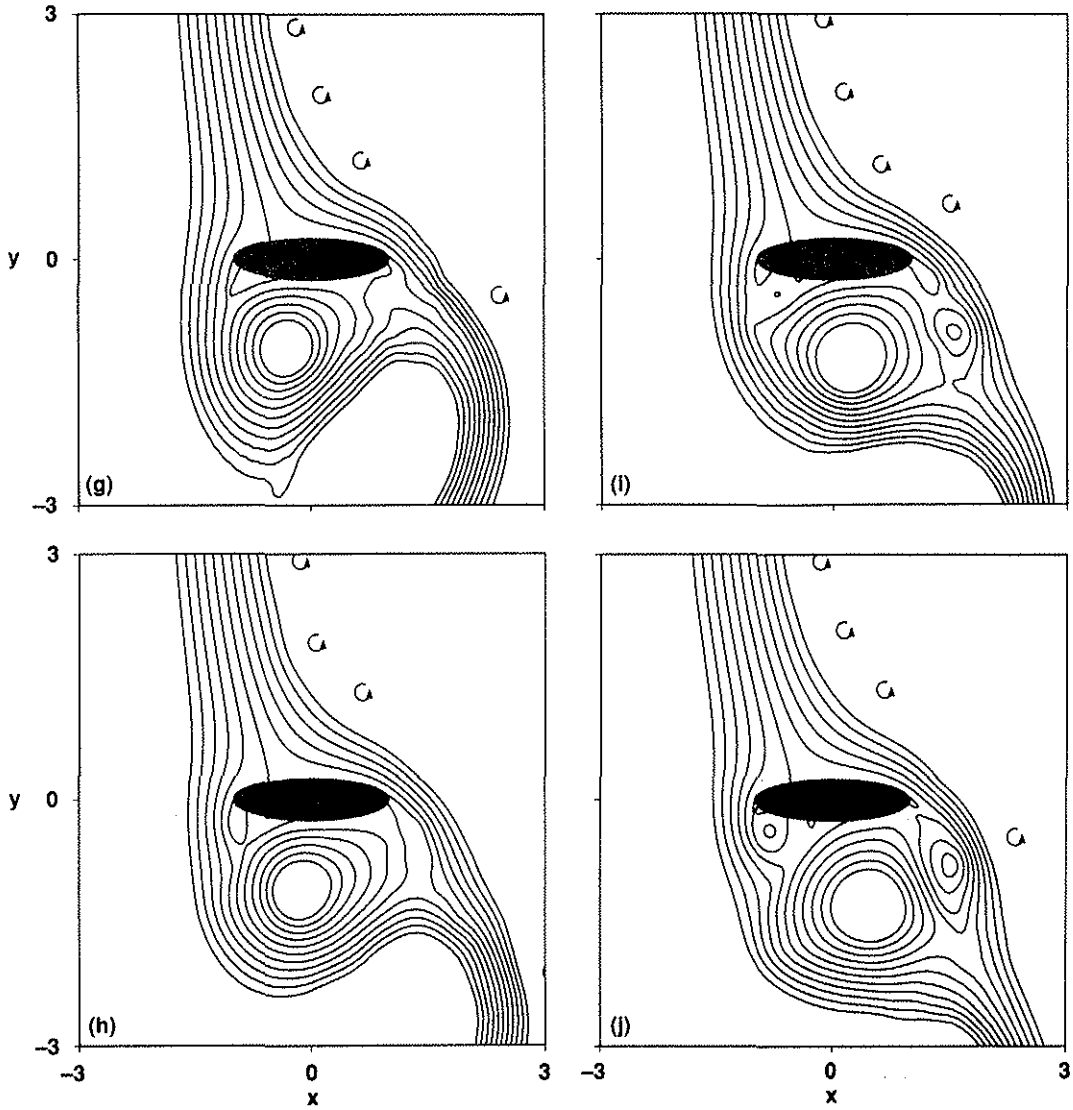

Fig 24 Concluded. (g) t = 7.0, (h) t = 8.0, (i) t = 9.0, (j) t = 10.0.